Modelling unsaturated soils with the Material Point Method. A discussion of the state-of-the-art[★]

Alba Yerro[a], Veronica Girardi[b], Francesca Ceccato[b], Mario Martinelli[c]

[a]*Virginia Tech, Department of Civil and Environmental Engineering, Blacksburg, VA, US*

[b]*University of Padua, Department of Civil, Environmental and Architectural Engineering, Padua, Italy*

[c]*Deltares, Delft, The Netherlands*

Abstract

Many natural hazards involve large deformations of unsaturated soils, e.g. rainfall-induced landslides, embankment collapses due to wetting, seepage-induced instabilities of dams and levees, etc. The study of these phenomena requires accounting for the complex hydro-mechanical interactions between solid skeleton and pore fluids and modeling large deformations to predict the post-failure behaviour, which poses significant computational challenges. In recent years, several hydro-mechanical coupled MPM formulations were developed to model saturated and unsaturated soils. These approaches are slightly different in terms of governing equations, integration schemes and have been implemented in different MPM software; thus, they benefit from various computational features. The purpose of this paper is to present an overview of the available MPM approaches to model unsaturated soils discussing differences and similarities of the formulations and their impact on the results under different conditions in a range of geotechnical appli-

---

cations. In addition, the effect of partially saturated conditions on the critical time step in explicit numerical integration schemes is studied for the first time. Different analytical expressions are derived and compared with the numerical results.

1. Introduction

Many geotechnical applications involve multi-phase interactions and large deformations of the ground. This is the case of rainfall-induced landslides, embankment collapses due to seepage or wetting, shallow foundation stability, and penetration problems in unsaturated soils, etc. Soil is a mixture of solid grains and pore fluids (liquid and/or gas) that interact with each other. In some cases, e.g. when considering dry or saturated soils in fully drained or fully undrained conditions, the interactions among the different phases can be simplified or even neglected. However, when the soil is in partially saturated conditions (i.e. gas and liquid coexist in the pores) or in saturated conditions when simultaneous generation and dissipation of fluid pore pressure is present, the mechanical and hydraulic response of the soil is fully controlled by the coupling between pore fluids and solid skeleton controls. Hence, the hydromechanical interactions need to be considered to accurately capture the material behaviour. The numerical analysis of these problems requires implementing multi-phase formulations and the consideration of appropriate boundary conditions (BCs) that can reproduce realistic scenarios of water infiltration, seepage, ponding, and changes in the water table.

Historically, fully-coupled hydro-mechanical formulations have been developed and adapted to traditional numerical frameworks such as finite elements (FEM)

2

and finite differences (FDM) methods. However, it is well known that these tools are limited to modeling relatively small deformations because of mesh tangling limitations. Alternatively, the numerical tools used for the analysis of post-failure runouts (i.e. propagation models) typically use rheological models that are difficult to trace back to soil's pre-failure conditions and commonly rely on depth-averaged integration schemes that cannot capture the failure initiation [1, 2, 3]

Several techniques have been proposed to overcome such difficulties e.g. A ArbitaryLagrangian Eulerian (ALE), Coupled Eulerian – Lagrangian (CEL), Particle Finite Element Method (PFEM), Finite Element Method with Lagrangian Integration Points (FEMLIP), Smooth Particle Hydrodynamics (SPH), Material Point Method (MPM), etc [e.g. 4, 5, 6, 7, 8]. A review of these methods and their applicability for the study of landslide mass movements can be found in [9]. Among them, the Material Point Method (MPM) has recently increased its popularity in the geotechnical community. The MPM is a particle-based numerical method especially well suited for the simulation of large deformations in history-dependent materials. It was initially developed in the framework of fluid mechanics under the name of Particle-In-Cell method (PIC) by Harlow [10] in Los Alamos National Laboratory. The basis of the method was to represent the flow of a continuum mass by a collection of material points (MPs) that moved through a background fixed mesh. It was not until 1994 that Sulsky et al. [8] extended the concept to solid mechanics for single-phase materials. During the last twenty years, MPM has been increasingly applied in the geotechnical engineering field for the study of soils and granular earth material. In particular, slope instabilities, failure of earth retaining structures, tunneling and underground collapses, soil penetration testing, pile installation, scour, internal erosion, among others [e.g. 11, 12, 13, 14, 15, 16, 17].

3

Different MPM coupled multi-phase formulations have been developed to address hydro-mechanical interactions between the solid skeleton and pore fluids. These approaches are slightly different in terms of governing equations, integration schemes, and they benefit of different computational features. In particular, this paper addresses the challenges of modeling hydro-mechanical interactions and large deformations of unsaturated soils using the MPM framework. The objectives are to provide an overview and discuss the available MPM approaches to model solid-liquid-gas mixtures, highlighting differences and similarities of the formulations, implementation aspects, and boundary conditions. Particular attention is paid to explain the relevance and physical meaning of common simplifications and their implications for the use of these approaches in practical applications. For the first time, the effect of partially saturated conditions on the time step in explicit MPM numerical integration schemes is studied. A set of analytical expressions for the critical time step are derived and compared with numerical results. Additionally, a discussion on existing applications is provided and the preliminary results of potential future applications is presented.

The paper is organized into four different sections. First, the MPM formulations are presented and discussed. Secondly, different implementation aspects are examined including boundary conditions and critical time step. Then, an overview of geotechnical applications is presented. Finally, the conclusions are summarized.

2. MPM formulations for unsaturated soils

Unsaturated porous media consist of a combination of three phases (ph): solid (S), liquid (L), and gas (G). The phases interact with each other determining the mechanic and hydraulic behaviour of the material. The solid phase is made of

4

solid grains that constitute the solid skeleton while the fluid phases (i.e. liquid and gas) fill the pore space.

In MPM, the material is considered as a continuum and is represented by a finite number of material points (MPs) that move together with the reference domain carrying all the information (e.g. stress, strain, mass, constitutive state variables). The computational cycle is summarized in Fig. 1. At the beginning of each time step, information carried by MPs is mapped to the nodes of the computational mesh and nodal mass, nodal velocities, forces, and dragging terms are evaluated. The main governing equations, usually the momentum balances, are solved in terms of main unknowns, typically acceleration or velocity. The nodal solution is interpolated using shape functions and the kinematic quantities and position of the MPs are updated accordingly. Finally, strains and stresses among other quantities are evaluated at the MPs using compatibility equations, mass balances, and constitutive relationships. At the end of the computational cycle, the nodal information is generally discarded. These features make the MPM a powerful tool in geotechnics. MPM also suffers from numerical artifacts (e.g. cell-crossing instability, volumetric locking, sporadic occurrence of empty elements in the material domain). Many publications are available in the literature describing the MPM algorithm and the numerical solutions to address its limitations (the reader is directed to [18] for an overview).

Two MPM frameworks have been presented to study multi-phase problems [19]: the single-point approach and the multi-point approach. The single-point framework represents the multi-phase soil mixture as a unique continuum represented with one set of MPs. During the calculation, all MPs move with the displacement of the solid skeleton represented using Lagrangian formulation and consequently
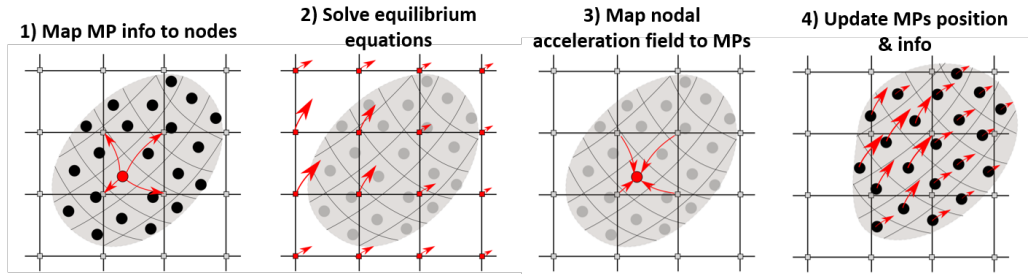
5

Fig. 1. Diagram of the MPM computational cycle (modified from [22]).

the solid mass in the MP remains constant. Fluids are allowed to flow in and out of the reference porous domain and their motion is described with respect to the moving solid skeleton. The single-point approach is the general framework selected to represent soils in unsaturated conditions as discussed herein. The multi-point framework requires more than one set of MPs to represent different phases. In particular, the double-point approach for saturated soil is available in the literature and represents solid skeleton and liquid with two completely separate sets of MPs [e.g. 20, 21]. Each set of MPs moves accordingly to the displacement of the corresponding phase and carries the information of one phase only, hence solid and fluid are represented using Lagrangian formulation. In the double-point configuration presented in [20, 21], the soil is considered either fully dry or fully saturated but this same approach can be extended to include hydro-mechanical interactions resulting from partially saturated conditions. Based on the authors knowledge, the study of unsaturated soils using a three-point approach (i.e. three sets of MP for solid, liquid and gas) has never been attempted yet.

The aim of following subsections is to provide an overview of the MPM formulations available in the literature for the simulation of unsaturated soils, proposed by Yerro et al. [23], Yerro [24], Bandara et al. [25], Wang et al. [26, 27], Lei and

$_{112}$ Solowski [28], Lei et al. [16], Ceccato et al. [29, 30], Martinelli et al. [31]. A

$_{113}$ summary of the main features discussed below is provided in Tab. 1.

$_{114}$ The governing equations of a comprehensive hydro-mechanically coupled formu-

$_{115}$ lation for unsaturated soils in a continuum framework should consider the balance

$_{116}$ equations of the phases and the interactions among them. Additionally, compat-

$_{117}$ ibility equations and constitutive relationships are also required to complete the

$_{118}$ equations set. General assumptions considered in all MPM formulations presented

$_{119}$ below include: (a) solid grains are incompressible, (b) fluids are weakly compress-

$_{120}$ ible, (c) fluid flows are laminar (Darcy's law is valid for gas and liquid phases), (d)

$_{121}$ fluid convective terms are negligible, and (e) isothermal conditions.

2.1. Momentum balance equations

$_{123}$ The first MPM formulation for unsaturated soils was proposed by Yerro [24], Yerro

$_{124}$ et al. [23]. This is a three-phase single-point formulation and each MP represents

$_{125}$ the solid-liquid-gas mixture. The main governing equations posed at the nodes of

$_{126}$ the computational mesh are the linear momentum balances of the gas, liquid, and

$_{127}$ mixture (Eqs. 1, 2, and 3, respectively). The first two are posed per unit of fluid

$_{128}$ volume, while the mixture is posed per unit of total soil volume. This formulation

$_{129}$ is fully dynamic and all relative acceleration terms are fully accounted with the

$_{130}$ accelerations of each phase being the primary unknowns of the system, i.e. $\mathbf{a}_S$, $\mathbf{a}_L$

$_{131}$ and $\mathbf{a}_G$.

$$\rho_G \mathbf{a}_G = \nabla p_G - \mathbf{f}_G^d + \rho_G \mathbf{g} \tag{1}$$

$$\rho_L \mathbf{a}_L = \nabla p_L - \mathbf{f}_L^d + \rho_L \mathbf{g} \tag{2}$$

$$n_S \rho_S \mathbf{a}_S + n_L \rho_L \mathbf{a}_L + n_G \rho_G \mathbf{a}_G = \nabla \cdot \boldsymbol{\sigma} + \rho_m \mathbf{g} \tag{3}$$

7

Table 1. Summary of most relevant characteristics of currently available MPM formulations for unsaturated soils.

Formulation	Yerro et al. [23]	Yerro [24]	Bandara et al. [25]	Wang et al. [26, 27], Lee et al. [32], Ceccato et al. [33, 29], Lei and Solowski [28], Lei et al. [16]	Ceccato et al. [30]	Martinelli et al. [31]
Number of phases	solid-liquid-gas	solid-liquid-gas	solid-liquid (+ suction)	solid-liquid (+ suction)	solid-liquid (+ suction)	solid-liquid (+ suction)
Dynamics	Fully dynamic	Fully dynamic	Relative acceleration of the liquid is neglected	Fully dynamic	Fully dynamic	Fully dynamic
Main governing equations	momentum of the mixture, momentum of the liquid, momentum of the gas	momentum of the mixture, momentum of the liquid, momentum of the gas	momentum of the mixture, momentum of the liquid	momentum of the mixture, momentum of the liquid	momentum of the mixture, momentum of the liquid	momentum of the solid, momentum of the liquid
Principal unknowns	a_S, a_L, a_G	a_S, a_L, a_G	a_S, w	a_S, a_L	a_S, a_L	a_S, a_L
Mass exchange	Liquid-Gas	Liquid-Gas	No	Solid-Liquid	No	No
Stress soil	Independent stress variables	Independent stress variables	Bishop effective stress	Bishop effective stress	Bishop effective stress	Bishop effective stress
Main hypothesis						
Incompressible solid grains	x	x	x	x	x	x
Weakly compressible fluids	x	x	x	x	x	x
Laminar fluid flow (Darcy's law)	x	x	x	x	x	x
Isothermal conditions	x	x	x	x	x	x
Solid-fluid relative acceleration is neglected			x			
Gas pressure is neglected			x	x	x	x
Gas density is neglected			x	x	x	x
Gradient of degree of saturation is negligible	x			x		x
Gradient of porosity is negligible	x			x		x
Gradient of liquid density is negligible	x			x		x

8

Where n_S, n_L and n_G are the volumetric concentration ratio of solid, liquid, and gas; ρ_S, ρ_L, ρ_G are densities of all phases and ρ_m is density of the mixture ($\rho_m = n_S\rho_S + n_\mathrm{L}\rho_\mathrm{L} + n_G\rho_G$); $\mathbf{f}_G^d$ and $\mathbf{f}_L^d$ are gas and liquid drag forces; p_G and p_L are gas and liquid pressures; σ is the total stress tensor; and $\mathbf{g}$ is the gravity vector. The porosity of the solid skeleton becomes $n = n_L + n_G$, and the volumetric concentration ratio of the fluid phases can be expressed in terms of the degree of saturation (S_L) and porosity as $n_L = nS_L$ and $n_G = n(1 - S_L)$, respectively for liquid and gas. Note that fully saturated conditions are the particular case when the degree of saturation S_L is one.

The fluid flow (either liquid or gas) is assumed laminar and the liquid and gas drag forces ($\mathbf{f}_G^d$ and $\mathbf{f}_L^d$) are written taking into account that Darcy's law is valid (Eq. 4). The subscript f denotes fluid phase, that can be either gas G or liquid L.

$$\mathbf{f}_f^d = \frac{n_f \mu_f}{k_f}(\mathbf{v}_f - \mathbf{v}_S) \tag{4}$$

Where μ_f and k_f correspond to the viscosity and intrinsic permeability of the fluids (i.e. $f = G, L$). The intrinsic permeability is defined in terms of hydraulic conductivity (κ_f) as

$$k_f = \kappa_f \frac{\mu_f}{\rho_f g} \tag{5}$$

The three momentum balances are integrated into the domain and discretised at the nodes of the computational mesh (the detailed expressions can be found in [24, 23]). At the beginning of each computational cycle, information carried by the MPs is mapped to the mesh to calculate nodal mass, nodal velocities, internal

9

and external forces, and dragging terms. Nodal gas and liquid accelerations are obtained first from solving the discretised version of Eqs. 1 and 2 independently. Finally, the nodal acceleration of the solid skeleton is obtained by solving Eq. 3 and using updated nodal fluid velocities.

The rest of the MPM formulations addressing unsaturated conditions assume that the density and pressure of the gas phase are negligible ($\rho_G = 0$ and $p_G = 0$). These formulations are essentially two-phase approaches that account for the suction effect. In consequence, the linear momentum balance of the gas is dropped from the system of equations and only two momentum balance equations are considered instead of three. This simplification reduces the computational cost. In the formulations proposed by Wang et al. [26, 27], Lei and Solowski [28], Lee et al. [32], Lei et al. [16], Ceccato et al. [29, 30] all dynamic terms, i.e. liquid and solid inertia, are considered and the main unknowns of the system are the accelerations of the solid and liquid phases ($\mathbf{a}_S$ and $\mathbf{a}_L$). The linear momentum of the liquid is identical to Eq. 2. The linear momentum of the mixture is equivalent to Eq. 3 but removing the dynamic term corresponding to the gas phase, which yields Eq. 6.

$$n_S\rho_S\mathbf{a}_S + n_L\rho_L\mathbf{a}_L = \nabla \cdot \boldsymbol{\sigma} + \rho_m\mathbf{g} \tag{6}$$

Very similarly, the formulation from Martinelli et al. [31] considers all dynamic terms and the solid and liquid accelerations as primary variables, but the momentum balance of the solid per unit of total volume (Eq. 7) is posed instead of the momentum balance of the mixture. $\mathbf{I}$ is the identity matrix.

$$n_S\rho_S\mathbf{a}_S = \nabla \cdot (\boldsymbol{\sigma} - n_L p_L\mathbf{I}) + (\rho_m - n_L\rho_L)\mathbf{g} + \mathbf{f}_L^d \tag{7}$$

10

171 Finally, the formulation by Bandara et al. [25] neglects the relative acceleration of

172 the liquid with respect to the solid skeleton. Therefore, all phases have the same

173 acceleration $\mathbf{a}$ (i.e. acceleration of the system, $\mathbf{a} = \mathbf{a}_S = \mathbf{a}_L$). The momentum

174 balances of the liquid, which is equivalent to the generalized Darcy equation

175 (Eq. 8), and the mixture (Eq. 9) are the governing equations posed at the nodes of

176 the computational mesh and the main unknowns are the acceleration of the system

177 $\mathbf{a}$ and the liquid seepage velocity ($\mathbf{w} = nS_L(\mathbf{v}_L - \mathbf{v}_S)$).

$$\mathbf{w} = -\frac{\kappa_L}{\mu_f}(\nabla p_L + \rho_L - \rho_L \mathbf{g}) \tag{8}$$

$$\rho_m \mathbf{a}_S = \nabla \cdot \boldsymbol{\sigma} + \rho_m \mathbf{g} \tag{9}$$

178 *2.2. Mass balance equations*

179 Additional governing equations include the mass balances. In the three-phase

180 MPM formulation [23, 24] the liquid and gas are considered to be a mixture of

181 water and air, and mass exchange between liquid and gas phases is allowed to

182 account for "water vapour" in the gas and "dissolved gas" in the liquid. The

183 process of mass exchange is not included herein to facilitate the reading of the

184 paper. Assuming incompressible solid grains ($\frac{D^S \rho_S}{Dt} = 0$), the expressions for the

185 mass balance of the solid and fluids (i.e. liquid and gas) phases are written as

186 Eqs. 10 and 11, respectively. $\frac{D^S(\bullet)}{Dt}$ is the material derivative with respect to the

187 solid motion.

$$\frac{D^S n}{Dt} - (1 - n)\nabla \cdot \mathbf{v}_S = 0 \tag{10}$$

$$n\frac{D^S(\rho_f S_f)}{Dt} + \nabla \cdot (\rho_f S_f n(\mathbf{v}_f - \mathbf{v}_S)) + \rho_f S_f \nabla \cdot \mathbf{v}_S = 0 \tag{11}$$

11

The mass balance of the solid (Eq. 10) represents the variation of porosity n caused by volumetric deformation of the solid skeleton. In those problems where the spatial variations of fluids mass in the soil are small ($\nabla(\rho_f S_f n) \approx 0$), Yerro et al. [23] simplify the term with the gradient of the advective fluxes of the fluid phases (i.e. $\nabla \cdot (\rho_f S_f n(\mathbf{v}_f - \mathbf{v}_S))$) yielding to Eq. 12. The effect of neglecting part of the advective flow gradients is further discussed in Sec. 2.5.

$$n\frac{\mathrm{D}^S(\rho_f S_f)}{\mathrm{D}t} + \rho_f S_f n\nabla \cdot (\mathbf{v}_f - \mathbf{v}_S) + \rho_f S_f \nabla \cdot \mathbf{v}_S = 0 \qquad (12)$$

The solid material derivatives from Eqs. 11 and 12 are evaluated using the chain rule and considering the fluid pressures (p_G and p_L) as state variables (Eq. 13). The fluid mass balances are solved in the MPM computational cycle in terms of the variation of liquid and gas pressure ($\frac{\mathrm{D}^S p_L}{\mathrm{D}t}$ and $\frac{\mathrm{D}^S p_G}{\mathrm{D}t}$).

$$\frac{\mathrm{D}^S(\rho_f S_f)}{\mathrm{D}t} = \left(S_f\frac{\partial \rho_f}{\partial p_L} + \rho_f\frac{\partial S_f}{\partial p_L}\right)\frac{\mathrm{D}^S p_L}{\mathrm{D}t} + \left(S_f\frac{\partial \rho_f}{\partial p_G} + \rho_f\frac{\partial S_f}{\partial p_G}\right)\frac{\mathrm{D}^S p_G}{\mathrm{D}t} \qquad (13)$$

The two-phase MPM formulations neglect the gas density and only the mass balances of the solid and liquid phases are required. All approaches consider the mass balance of the solid as presented in Eq. 10, but propose slightly different versions of the mass balance of the liquid. Ceccato et al. [30] consider the liquid mass balance with no simplification regarding the the gradient of the advective fluxes, leading to Eq. 14. Wang et al. [26, 27], Ceccato et al. [33, 29], Lee et al. [32], Martinelli et al. [31] neglect the gradients of the liquid mass ($\nabla(\rho_L S_L n) \approx 0$) and use Eq. 15 instead. Bandara et al. [25] rewrites Eq. 14 in terms of $\mathbf{w}$.

$$n\frac{\mathrm{D}^S \rho_L S_L}{\mathrm{D}t} = -\nabla \cdot (\rho_L S_L n(\mathbf{v}_L - \mathbf{v}_S)) - \rho_L S_L \nabla \cdot \mathbf{v}_S \tag{14}$$

$$n\frac{\mathrm{D}^S \rho_L S_L}{\mathrm{D}t} = -\rho_L S_L n\nabla \cdot (\mathbf{v}_L - \mathbf{v}_S) - \rho_L S_L \nabla \cdot \mathbf{v}_S \tag{15}$$

The solid material derivatives from Eqs. 14 and 15 are evaluated assuming a weakly-compressible liquid (see Sec. 2.4.2), and the variation of the liquid pressure $(\frac{\mathrm{D}^S p_L}{\mathrm{D}t})$ is derived accordingly.

$$\frac{\mathrm{D}^S \rho_L S_L}{\mathrm{D}t} = \rho_L \frac{\mathrm{D}^S S_L}{\mathrm{D}t} - \frac{\rho_L}{K_L}\frac{\mathrm{D}^S p_L}{\mathrm{D}t} \tag{16}$$

Finally, the formulation proposed by Lei and Solowski [28], Lei et al. [16] extends the previous works to account for internal erosion of the solid skeleton, based on the work from Yerro et al. [34] for saturated conditions. The mass exchange between the solid and liquid phases is allowed according to an erosion law that controls the rate of eroded mass. This implies that the mass balances of solid and liquid phases (Eq. 10 and Eq. 14) are extended with an additional term to account for the lost or gained mass, respectively. In this formulation, the gradient of the liquid density is neglected, but gradients of porosity and degree of saturation are accounted. In addition to the solid and liquid mass balances, the mass balance of the eroded grains (i.e. liquidized spices) is also required in the system.

2.3. Compatibility equations

All formulations consider the same compatibility equations to obtain the infinitesimal strain rate tensor of each phase $\boldsymbol{\varepsilon}_{ph}$ (i.e. $ph = S, L, G$) at the MPs. These can be written in terms of the corresponding phase velocities as in Eq. 17. In the

13

₂₂₃ MPM computational cycle, the compatibility equation is evaluated at the MPs and

₂₂₄ updated nodal velocities are considered to calculate the corresponding gradients.

$$\frac{\mathrm{D}^S \boldsymbol{\varepsilon}_{ph}}{\mathrm{D}t} = \frac{1}{2}\left[\nabla \cdot \mathbf{v}_{ph} + (\nabla \cdot \mathbf{v}_{ph})^T \right] \tag{17}$$

₂₂₅ *2.4. Constitutive laws*

₂₂₆ Different constitutive laws are required to complete the set of governing equations.

₂₂₇ These are evaluated at the MPs, generally at the end of the computational cycle.

₂₂₈ *2.4.1. Stress-strain relationship for solid skeleton*

₂₂₉ The relationship between the strains of the solid skeleton and the stress is defined

₂₃₀ by means of a constitutive equation. Various hydro-mechanical stress frameworks

₂₃₁ are available in the literature to describe the behaviour of unsaturated soils [35].

₂₃₂ They are inherited from the Bishop single effective stress approach [36] or from the

₂₃₃ independent stress variable approach [37]. The Bishop effective stress approach is

₂₃₄ the most commonly implemented in the MPM formulations [25, 27, 16, 32, 30, 31].

₂₃₅ The general form of the constitutive equation is presented incrementally as Eq. 18,

₂₃₆ where the effective stress essentially controls the stress state of unsaturated soil

₂₃₇ and is defined as Eq. 19. $\mathbf{D}$ is the tangent matrix, $\boldsymbol{\varepsilon}$ is the strain vector of the

₂₃₈ solid skeleton, $\boldsymbol{\sigma}_{net}$ is the net stress ($\boldsymbol{\sigma}_{net} = \boldsymbol{\sigma} - p_G \mathbf{I}$), s is the matric suction

₂₃₉ ($s = p_G - p_L$), and χ is an effective stress parameter generally assumed equal to

₂₄₀ S_L. Note that most of the works assume $p_G = 0$.

$$d\boldsymbol{\sigma}' = \mathbf{D} \cdot d\boldsymbol{\varepsilon} \tag{18}$$

$$\boldsymbol{\sigma}' = \boldsymbol{\sigma}_{net} - \chi s \mathbf{I} \tag{19}$$

14

The independent stress variable approach is used in [23], where the net stress is defined more generally as Eq. 20. In this context, the stress state is described by two state variables (i.e. $\boldsymbol{\sigma}_{net}$ and s) and a double constitutive matrix is required (Eq. 21), where **h** is a constitutive vector controlling the influence of suction.

$$\boldsymbol{\sigma}_{net} = \boldsymbol{\sigma} - \max\{p_G, p_L\}\mathbf{I} \tag{20}$$

$$d\boldsymbol{\sigma}_{net} = \mathbf{D} \cdot d\boldsymbol{\varepsilon} + \mathbf{h}ds \tag{21}$$

Very limited number of constitutive models have been considered in both stress frameworks. Linear elasticity has been used for validation purposes and the standard elastic-perfectly plastic Mohr Coulomb and the Mohr Coulomb with suction hardening [38] have also been used for the study of different failure problems (Sec. 4 includes a review of the applications). Finally, the Jaumann stress rate is adopted in case of large deformation to achieve objectivity (i.e. frame indifferent formulation) of the Cauchy stress rate matrix [25, 31].

2.4.2. Weakly-compressible fluids

All the currently available MPM formulations for unsaturated soils consider linear elastic weakly-compressible fluids (Eq. 22), where K_f is the bulk modulus of the reference fluid.

$$-\frac{1}{\rho_f}\frac{\partial \rho_f}{\partial t} = \frac{1}{K_f}\frac{\partial p_f}{\partial t} \tag{22}$$

2.4.3. Soil water retention curve

The soil water retention curve (SWRC) is an essential relationship required to model the behaviour of unsaturated soils that correlates suction ($s = p_G - p_L$) with

15

259 degree of saturation (S_L). For the purpose of simulating realistic soil behaviour,
260 the Van Genuchten SWRC [39] (Eq. 23) is preferred among the authors, where
261 p_0 and λ are fitting parameters. Alternatively, a linear SWRC (Eq. 24) is also
262 employed for validation purposes, where a_v is a constant parameter, S_{min} is the
263 residual degree of saturation, and S_{max} is the maximum degree of saturation.

$$S_L = S_{min} + (S_{max} - S_{min}) \left[1 + \left(\frac{p_G - p_L}{p_0} \right)^{\frac{1}{1-\lambda}} \right]^{-\lambda} \tag{23}$$

$$S_L = 1 - a_v(p_G - p_L) \tag{24}$$

2.4.4. Liquid relative hydraulic conductivity

265 It is well known that unsaturated soils are less permeable than fully saturated
266 soils. The liquid relative hydraulic conductivity (i.e. the ratio between the actual
267 liquid hydraulic conductivity and the saturated hydraulic conductivity, κ_L/κ_{sat})
268 is a function of the degree of saturation. This dependence is also included in
269 the MPM formulations with the introduction of the hydraulic conductivity curve
270 (HCC). The most common HCC are the functions proposed by Hillel [40] (Eq. 25),
271 and Mualem [41] (Eq. 26), where r and λ are fitting parameters.

$$\frac{\kappa_L}{\kappa_{sat}} = S_L^r \tag{25}$$

$$\frac{\kappa_L}{\kappa_{sat}} = \sqrt{S_L} \left[1 - \left(1 - S_L^{\frac{1}{\lambda}} \right)^\lambda \right]^2 \tag{26}$$

2.5. Discussion

273 This section discusses the effect of the gradient of advective fluxes in the fluid
274 mass balance equations. Eq. 11 can be written as Eq. 27, where $f = L, G$, by
275 expanding the gradient of the advective flux term.

16

$$n\frac{\mathrm{D}^S(\rho_f S_f)}{\mathrm{D}t} + \nabla(\rho_f S_f n) \cdot (\mathbf{v}_f - \mathbf{v}_S) + \rho_f S_f n \nabla \cdot \mathbf{v}_f + \rho_f S_f (1-n) \nabla \cdot \mathbf{v}_S = 0 \quad (27)$$

The first addend is related to the liquid mass change as a result of pressure and degree of saturation variation in time (Eq. 16). All other terms explain the variation of liquid mass as a result of the liquid inflow/outflow gradients resulting from different mechanisms. In particular, the second term in Eq. 27 describes the variation of the liquid mass induced by a flow triggered by the fluid mass gradient; the third term describes the variation of liquid mass due to the divergence of the fluid velocity (equivalent to a volumetric deformation of the fluid); and the fourth term describes the variation of liquid mass due to the divergence of the solid velocity (equivalent to a volumetric deformation of the solid skeleton).

The mass balance equation is solved at the MP level, where the computation of the last two terms of Eq. 27 is straightforward because nodal velocities are already available during the traditional computational cycle. In contrast, the evaluation of the fluid mass gradient requires the additional step of mapping the quantity $\rho_f S_f n$ to the nodes and then calculate the gradient at the MP [24]. This is relatively simple and does not increase significantly the computational cost. The gradient of fluid mass can be calculated as Eq. 28. While the spatial gradient of liquid density ($\nabla \rho_f$) and porosity (∇n) can be assumed negligible in most cases, the gradient of the degree of saturation depends on the pressure gradient and the SWRC. The importance of the last term of Eq. 28 increases with pressure gradient and $\partial S_f / \partial p_f$.

$$\nabla(\rho_f S_f n) = S_f n \nabla \rho_f + S_f \rho_f \nabla n + n \rho_f \nabla S_f \quad (28)$$

17

To visualize the effect of this term, the evolution of suction in a 1m soil column during an infiltration test is considered. For $t = 0$, an initial suction s_0 is applied along the column. For $t > 0$, zero suction is imposed at the top boundary while the bottom is impervious. Gravity is neglected. The soil permeability is constant and the SWRC is linear (Eq. 24). Under these assumptions, an analytical expression that describes the evolution of the normalized suction along the column with time can be derived from the mass balance equation of the liquid following [42]

Numerical simulations are performed with the two-phase formulations for unsaturated soils with the material parameters listed in Tab. 2.

Figure 2 compares the results obtained with the complete mass balance equation (Eq. 14, circles) and with the simplified mass balance equation (Eq. 15, cross symbol) considering different values of initial suction s_0 and $\partial S_L/\partial p_L = a_v$. For $s_0 = 500 kPa$ and $a_v = 1 \cdot 10^{-3}$ (Fig. 2a) the simplified mass balance equation leads to a delay in the evolution of suction, while the complete mass balance equation gives results in very good agreement with the analytical solution. Decreasing the slope of the SWRC to $a_v = 1 \cdot 10^{-5}$ (Fig. 2b) or reducing the initial suction to $s_0 = 5 kPa$, i.e. the pressure gradient, (Fig. 2c) the two approaches give very similar results. Indeed, in these cases, the contribute of the last term of Eq. 28 is very small and neglecting the gradient of fluid mass is an acceptable simplification. For the range of pressure gradients and SWRC typical of many civil engineering applications the error introduced using Eq. 15 is acceptably small.

Similar results are obtained with the three-phase formulation as discussed in [43].

18

Solid density [kg/m^3]	ρ_S	2700
Liquid density [kg/m^3]	ρ_L	1000
Porosity [-]	n	0.4
Liquid bulk modulus [kPa]	K_L	80000
Liquid dynamic viscosity [$kPa \cdot s$]	μ_L	$1 \cdot 10^{-6}$
Intrinsic permeability liquid [m^2/s]	κ_L	$1 \cdot 10^{-11}$

Table 2. Material parameters for 1D infiltration example with applied pressure.
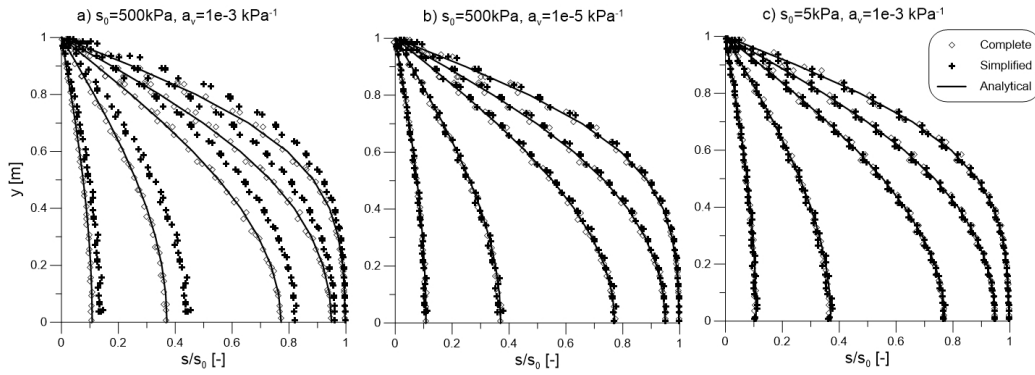
Fig. 2. Evolution of normalized suction with depth. Comparison between numerical and analytical formulations.

3. Implementation aspects

This section presents an overview of different implementation aspects concerning unsaturated MPM formulations such as the stability of the solution and the application of boundary conditions.

3.1. Time integration scheme and critical time step

All MPM formulations presented for the study of unsaturated soils are based on numerical schemes explicitly integrated in time. Commonly, the Euler-Cromer

19

algorithm is used. Explicit schemes are conditionally stable depending on a maximum or critical time step Δt_c, that depends on the material properties and characteristic size of the computational grid. According to the authors' knowledge, no studies have been performed concerning the effects of partially saturated conditions on Δt_c.

3.1.1. Review of stability criteria

In two-phase problems we can define two time scales of interest, namely that of excess pore pressure dissipation related to consolidation and infiltration and that of compression wave propagation within the solid-fluid mixture. In mathematics, consolidation (infiltration) is seen as parabolic behaviour, while wave propagation is hyperbolic behaviour. The associated critical time steps are expresses by Eq. 29 and Eq. 30 respectively, where L_i is a characteristic length, i.e. the size of an element.

$$\Delta t_c = \frac{L_i^2}{2c} \tag{29}$$

$$\Delta t_c = \frac{L_i}{v_c} \tag{30}$$

The coefficient c can be written as Eq. 31 where E_c' is the effective oedometric modulus. Note that for $S_L = 1$ and $\frac{dS_L}{ds} = 0$ it coincides with the consolidation coefficient.

$$c = \frac{k_L}{\mu_L\left(\frac{1}{E_c'} + \frac{S_L n}{K_L} + n\frac{dS_L}{ds}\right)} \tag{31}$$

v_c in Eq. 30 represents the one-dimensional compressing wave speed propagation

and can be estimated with Eq. 32, where E_c and ρ are the oedometric modulus and the density of the considered material.

$$v_c = \sqrt{\frac{E_c}{\rho}} \qquad (32)$$

Eq. 32 can be particularized for undrained conditions using $E_c = E'_c + n/K_L$ and $\rho = \rho_{sat}$ or for dry conditions using $E_c = E'_c$ and $\rho = \rho_{dry}$.

Yerro [24] and Mieremet [44] mathematically studied the stability of the two-phase MPM formulation for saturated conditions proposed in [45]. In the work of Yerro [24], the eigenvalue problem is solved to study the stability of four different equations: (a) the liquid momentum balance $\Delta t_{c,liquid}$, (b) the mixture momentum balance $\Delta t_{c,mixture}$, (c) the coupled hydro-mechanical system ($\Delta t_{c,coupled}$) (i.e. liquid and mixture momentum balances), and (d) the momentum balance of the mixture in undrained conditions ($\Delta t_{c,undrained}$). The critical time step criterion for the undrained analysis is identical to Eq. 30, while the other three criteria share the following expression

$$\Delta t_{c,Yerro} = \frac{2}{\omega}\left[-\xi + \sqrt{\xi^2 + 1}\right] \qquad (33)$$

where ω and ξ vary depending on the set of equations considered, and provided in Tab.3 (saturated column).

Mieremet [44] considered the stability of the coupled hydro-mechanical system concerning liquid and mixture momentum balances. Rigorous mathematical stability analysis were conducted by means of the matrix method [46], and an estimation of Δt_c is proposed as

21

$$\Delta t_{c,Mieremet} = \frac{-2a + \sqrt{4a^2 + 8(b + \sqrt{b^2 - 4d})}}{b + \sqrt{b^2 - 4d}} \tag{34}$$

where terms a, b and d are reported in Tab. 4 (saturated column). The performance of the proposed criterion is verified with 1D FEM-based simulations.

3.1.2. New stability criteria for unsaturated conditions

Assuming that saturation can be understood as a particular case of unsaturated conditions, one could expect that the Δt_c for unsaturated formulations is an extension of those obtained for saturated conditions. In this work, the stability of the MPM formulation proposed by Ceccato et al. [30] in unsaturated conditions is studied considering the same approach followed by Yerro [24]. The stability of (a) the momentum balance of the liquid, (b) the momentum balance of the mixture, and (c) the coupled system is derived. The main passages to obtain the stability criteria are presented in detail in the Appendix (Sec. 7). The obtained expressions for the critical time step follow the same structure as Eq. 33. The new terms ω and ξ are reported in Tab. 3 (unsaturated column).

Given the consistent complexities in applying the same rigorous procedure by Mieremet [44] to the formulation by Ceccato et al. [30], a simplified "adaptation" of Eq. 34 to unsaturated conditions is proposed. The terms a, b and d are modified in a similar manner to ω and ξ in saturated vs. unsaturated conditions (3). In the term a, S_L^2 is added and ρ_{sat} is replaced by ρ_m. In terms b and d, the liquid bulk modulus K_L is replaced by $\frac{S_L}{\left(\frac{dS_L}{ds}\right) + \frac{S_L}{K_L}}$, based on ω_C and ω_M unsaturated expressions. Note that, consistently for all the criteria, the saturated case ($S_L = 1$) is a particular case of the unsaturated expressions.

22

	Saturated	Unsaturated
Coupled	$\omega_C = \frac{1}{L_i}\sqrt{\frac{K_L}{\rho_L} + \frac{E_c}{\rho_S(1-n)} + \frac{(1-n)}{n}\frac{K_L}{\rho_S}}$	$\omega_C = \frac{1}{L_i}\sqrt{\left[\frac{S_L}{\left(\frac{dS_L}{ds}+\frac{S_L}{K_L}\right)}\right]\left[\frac{1}{\rho_L} + \frac{1}{\rho_S}\left(\frac{1}{n} - S_L\right)\right] + \frac{E_c}{\rho_S(1-n)}}$
	$\xi_C = \frac{n\mu_L}{2k_L\omega_C}\left[\frac{n}{(1-n)\rho_S} + \frac{1}{\rho_L}\right]$	$\xi_C = \frac{S_L n\mu_L}{2k_L\omega_C}\left[\frac{S_L n}{(1-n)\rho_S} + \frac{1}{\rho_L}\right]$
Liquid	$\omega_L = \frac{1}{L_i}\sqrt{\frac{K_L}{\rho_L}}$	$\omega_L = \frac{1}{L_i}\sqrt{\frac{S_L}{\rho_L\left(\frac{dS_L}{ds}+\frac{S_L}{K_L}\right)}}$
	$\xi_L = \frac{n\mu_L}{2k_L\omega_L}\frac{1}{\rho_L}$	$\xi_L = \frac{S_L n\mu_L}{2k_L\omega_L}\frac{1}{\rho_L}$
Mixture	$\omega_M = \frac{1}{L_i}\sqrt{\frac{E_c}{(1-n)\rho_S} + \frac{(1-n)}{n}\frac{K_L}{\rho_S}}$	$\omega_M = \frac{1}{L_i}\sqrt{\frac{1}{\rho_S}\left[\frac{E_c}{(1-n)} + \left(-S_L + \frac{1}{n}\right)\frac{S_L}{\left(\frac{dS_L}{ds}+\frac{S_L}{K_L}\right)}\right]}$
	$\xi_M = \frac{n^2\mu_L}{2(1-n)\rho_S k_L\omega_M}$	$\xi_M = \frac{S_L^2 n^2\mu_L}{2(1-n)\rho_S k_L\omega_M}$

Table 3. Parameters ω and ξ used in Δt_c expression by Yerro [24]. Left column: original version for saturated conditions. Right column: new development for unsaturated conditions.

	Saturated		Unsaturated
Mieremet	$a = \frac{n\rho_{sat}\mu}{(1-n)\rho_S\rho_L k_L}$	Mieremet$_{adapted}$	$a = \frac{S_L{}^2 n\rho_m\mu}{(1-n)\rho_S\rho_L k_L}$
	$b = \frac{4(n\rho_{sat}K_L+(1-2n)\rho_L K_L+n\rho_L E_c)}{n(1-n)\rho_S\rho_L L_i^2}$		$b = \frac{4\left(n\rho_m\frac{S_L}{\left(\frac{dS_L}{ds}+\frac{S_L}{K_L}\right)}+(1-2n)\rho_L\frac{S_L}{\left(\frac{dS_L}{ds}+\frac{S_L}{K_L}\right)}+n\rho_L E_c\right)}{n(1-n)\rho_S\rho_L L_i^2}$
	$d = \frac{16E_c K_L}{(1-n)\rho_S\rho_L L_i^4}$		$d = \frac{16E_c\frac{S_L}{\left(\frac{dS_L}{ds}+\frac{S_L}{K_L}\right)}}{(1-n)\rho_S\rho_L L_i^4}$

Table 4. Parameters a, b and d used in Δt_c expression by Mieremet [44]. Left column: original version for saturated conditions. Right column: adapted criterion for unsaturated conditions.

3.1.3. Numerical analysis and discussion

In this section, the performances of the unsaturated criteria are evaluated. A trial and error procedure is used to explore Δt_c in unsaturated conditions. A series of MPM-based simulations is performed with Anura3D [47] using the unsaturated formulation in [30]. The objective is to determine Δt_c for different degrees of saturation. The model is a soil column, 1m high and 0.05m wide. At the top of the column, an external load of 100kPa is applied, see Fig. 3 (a). An initial suction is imposed to the entire column and the same suction is applied at the top of the column during the rest of the calculation to ensure that the degree of saturation remains as constant as possible in the model. The material is linear elastic and the intrinsic permeability ($k_L = 2 \cdot 10^{-10} m^2$, equivalent to a hydraulic conductivity of $\kappa \approx 2 \cdot 10^{-3} m/s$) is assumed constant. The mesh is made by linear triangular elements of 0.05m side length. The bottom boundary is fully fixed and impervious. The lateral boundaries only allow vertical movement and are impervious.

The same analysis is repeated for three soil types (sand, silt, and clay) to evaluate the effect of the SWRCs on the numerical stability. The Van Genuchten model is used to describe three reference SWRC from [48] (Fig. 3 (b)). The SWRC parameters are provided in Tab. 5. The simulations are performed for each soil type ensuring a large range of suction values, covering degrees of saturation from saturated ($S_L = 1.0$) to approximately dry conditions ($S_L = 10^{-2}$).

Moreover, to evaluate the critical time step in diverse conditions we consider different sets of analysis varying the porosity ($n = 0.4$ and $n = 0.6$) and the Young modulus ($E_1 = 10^4 kPa$ and $E_2 = 5 \cdot 10^4 kPa$). The Poisson ratio is assumed constant for all the simulations, $\nu = 0.2$.

24
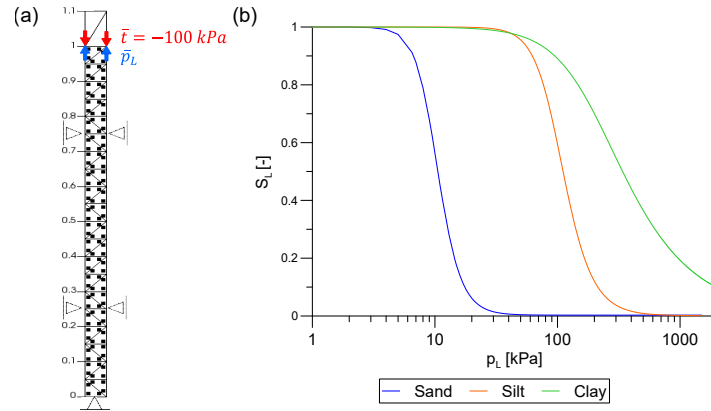
Fig. 3. Critical time step in unsaturated conditions obtained from numerical simulations: (a) geometry of the problem, (b) SWRCs tested.

The time step of each calculation is manually increased until the simulation doesn't converge. This iterative process is repeated for each combination of material parameters. The maximum value that ensures the solution convergence is considered the critical time step.

The critical time steps obtained from the numerical tests performed in sand, silt, and clay are presented in Fig. 4, Fig. 5 and Fig. 6, respectively. In all figures, the numerical results plotted together with the stability criteria proposed in this work for unsaturated conditions (Tab. 3 and 4). In addition, the expressions from the literature, i.e. consolidation and infiltration (Eq. 29), and CFL in undrained and dry conditions (Eq. 30) are also presented for reference. All the expressions are evaluated considering $L_i = 0.035m$ which corresponds to the minimum altitude of the element.

The numerical results show a general increase of Δt_c in the unsaturated regime.
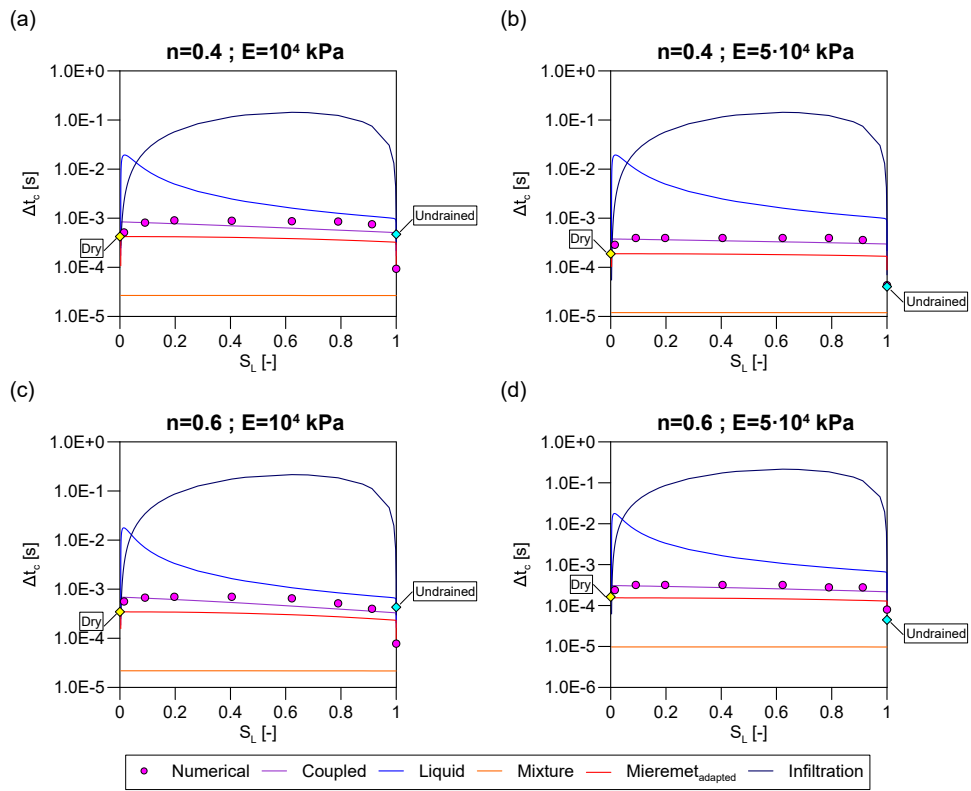
25

Fig. 4. Δt_c results from MPM simulations compared with mathematical expressions and literature criteria. Sand SWRC.
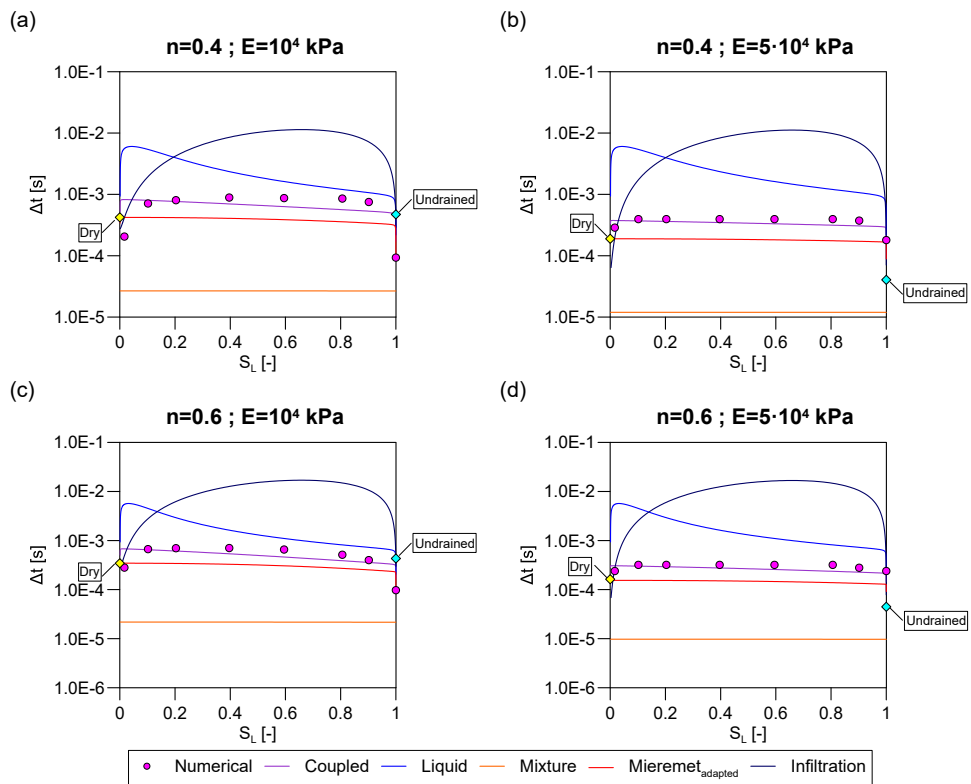
Fig. 5. Δt_c results from MPM simulations compared with mathematical expressions and literature criteria. Silt SWRC.
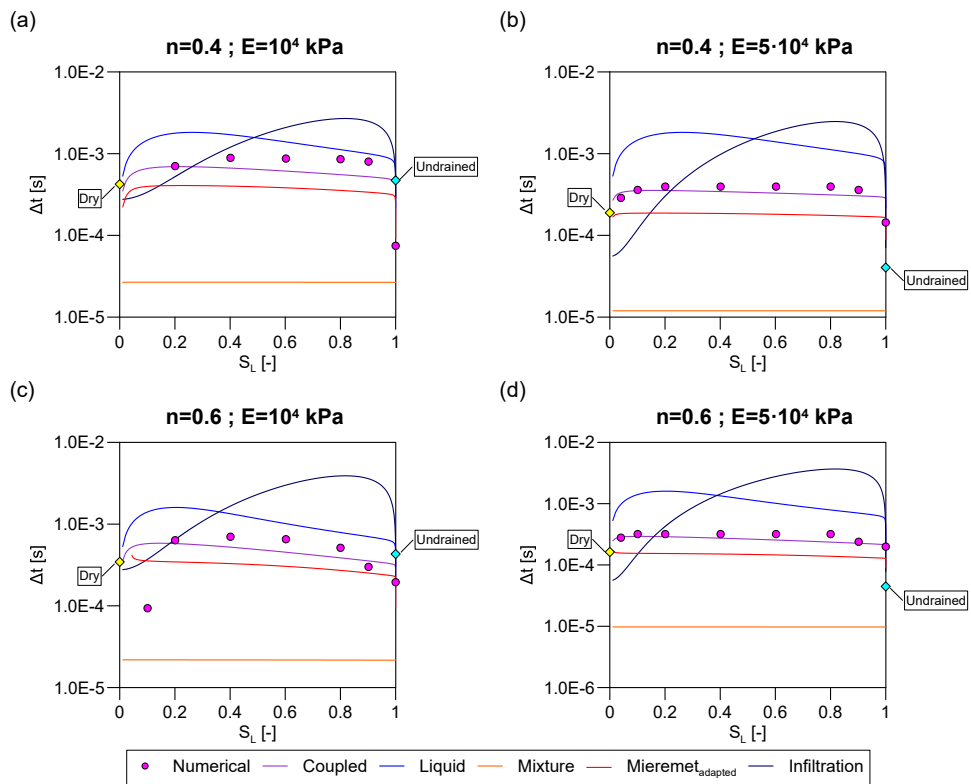
Fig. 6. Δt_c results from MPM simulations compared with mathematical expressions and literature criteria. Clay SWRC.

	Sand	Silt	Clay
S_{min} [-]	0.003	0.001	0.001
S_{max} [-]	1.0	1.0	1.0
p_{ref} [kPa]	9.9	100.0	196.0
λ [-]	0.8	0.75	0.5

Table 5. Van Genuchten parameters for the three SWRCs used in the critical time step numerical analysis.

419 The coupled criterion $\Delta t_{c,Coupled}$ appears as the one better fitting the results, 420 however, it overestimates Δt_c near the extremes (dry and saturated conditions). 421 $\Delta t_{c,Mieremet_{adapted}}$ is the second closest criterion, and it trends to be more con- 422 servative than $\Delta t_{c,Coupled}$. It is important to note that near the dry conditions 423 ($S_L \approx 10^{-2}$) a sharp decrease of Δt_c is consistently observed. This decrease is 424 highlighted by $\Delta t_{c,Coupled}$, $\Delta t_{c,Liquid}$ and $\Delta t_{c,Mieremet_{adapted}}$ criteria. It should be 425 noted that the use of $\Delta t_{c,Mieremet_{adapted}}$ is limited by negative values under the 426 square root present at the numerator of this expression (Eq. 34). This situation 427 seems to occur when suction values are extremely high (i.e. S_L is very low). 428 This behaviour occurs for silt SWRC when $s > 1800 kPa$ and for clay SWRC 429 when $s > 4500 kPa$ (although it is difficult to appreciate in the figures because 430 of the logarithmic scale). These values of suction are hardly encountered in real 431 geotechnical scenarios.

432 To better quantify the increase of Δt_c in unsaturated conditions and to visualize the 433 effect of each material parameter on it, in Fig. 7(a) the numerical Δt_c values are 434 normalized with respect to $\Delta t_{c,Mieremet}$ (criterion for saturated conditions, Eq. 34). 435 We can observe that smaller porosity values result in bigger Δt_c, as highlighted

29

by circle and diamond symbols. On the other side, the higher Young modulus results in lower Δt_c values, visible with square and cross symbols. Furthermore, the higher Young modulus gives a more flat trend in the interval between $S_L = 0.2$ and $S_L = 0.8$. It is interesting to observe the comparable (in some cases identical) increase in Δt_c among the different materials for the same combination of porosity and Young modulus. The major differences occur when approaching dry conditions.

In addition, in Fig.7(b), the outcomes using the same model scaled up 10 times, $L_i = 0.5m$ are introduced to emphasize the mesh size effect on Δt_c. This comparison is related to the silt material. It is clear that Δt_c depends on the mesh size. Results with the coarser mesh have a different trend of critical time step. The sharp reduction of Δt_c near dry conditions is no more present, on the contrary, in this normalization, Δt_c is continuously increasing and the two porosity values tested results in very similar results. A more extensive investigation in this regard is further necessary to understand the different behaviours.

These preliminary results can encourage future studies and provide an indicative support to stimulate researchers using MPM unsaturated formulations in testing higher values of Δt_c in situations where significant variations of S_L or extreme values in the unsaturated regime, i.e. full saturation or dry conditions, are not encountered. Further studies need to be performed to investigate the effect of other parameters such as permeability on the stability of the solution.

3.2. Boundary conditions

Given the multi-phase nature of the formulation, the boundary conditions (BCs) need to be applied on each phase separately (solid, liquid, and eventually gas).

30
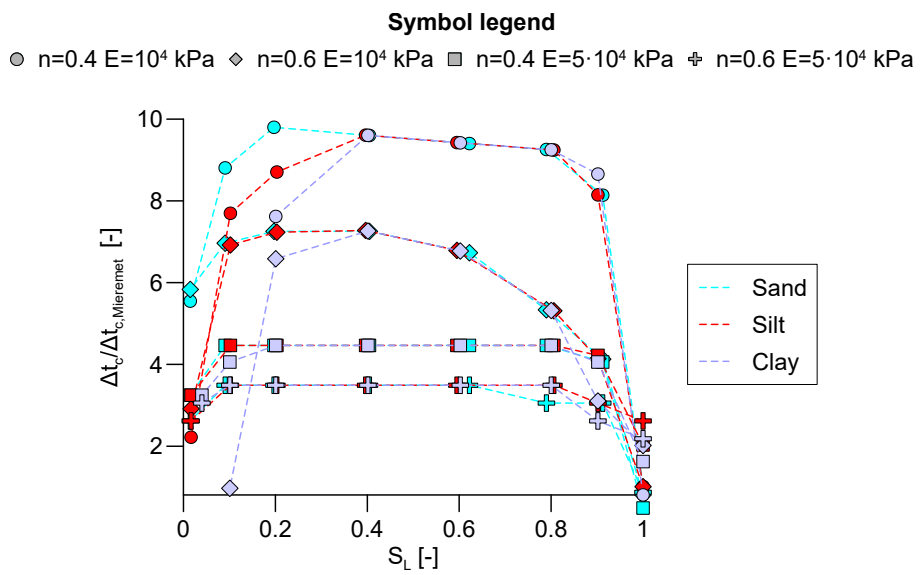
Fig. 7. Comprehensive numerical results normalized with respect to $\Delta t_{c,Mieremet}$, as function of saturation degree (a) ($L_i = 0.05m$). Comparison of normalized Δt_c for different mesh sizes using silt SWRC (b).
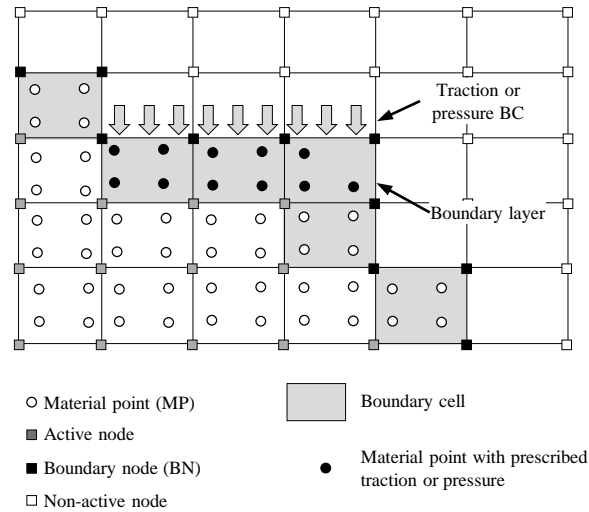
Fig. 8. BC applied with the *boundary layer* approach.

Two kinds of BCs can be distinguished – essential and natural. Essential BCs are imposed directly on the solution, and the degrees of freedom are eliminated from the system of equations. Fixities, prescribed accelerations, velocities, or displacements are typical examples of essential BCs. Natural BCs are imposed on a secondary variable, such as stresses or pressures, and they are included in the weak form of the governing equations. In classical FEM, the application of BCs is relatively simple as these can be specified directly on the boundary nodes, which coincide with the boundary of the continuum body, and are well defined throughout the computation. However, the computational mesh in MPM does not necessarily align with the boundary of the material making the application of the BCs more challenging.
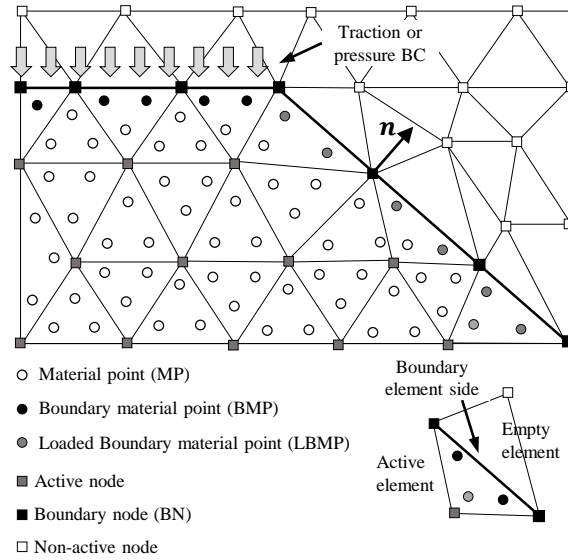
Fig. 9. BC applied at the boundary MP or at the boundary nodes.

Bandara et al. [25] apply the concept of *boundary layer* in which the applied traction or pressure is prescribed to all the MP inside the boundary cells. Boundary cells are those adjacent to empty cells, and they are determined at each time step (Fig. 8). The disadvantage of this approach is that traction (or pressure) is distributed over a thickness that has the size of the cell. In the Anura3D software [47] used by [23, 30, 32, 31] loads can be applied on either the boundary element side or the boundary material points (BMPs, Fig. 9) [49]. The first option is applicable only when the boundary of the body remains aligned with loaded element boundaries throughout the computation. The nodal traction force is integrated like in FEM applying Gauss quadrature and then used in the momentum balance equation. The applied load is thus integrated accurately, and the traction nodal force is non-zero only for the nodes belonging to the loaded surface. The

second option consists of storing the load on specific MPs (loaded BMP, LBMP) that can move through the mesh. This is mapped from LBMPs to all nodes of the element where it is located by means of the shape functions. In this way, the surface force is distributed across the layer of elements that borders the boundary, but the effect is less severe compared to the boundary layer approach. The LBMPs may move a long distance and become non-boundary material points, which may lead to unrealistic results.

An alternative definition of pressure BC is the *hydraulic head* BC, which is very useful to simulate, for example, water levels in reservoirs [30, 50]. A total head value $\widehat{H}$ is prescribed on the boundary, which is related to the applied pressure $\widehat{p}_L$ by means of Bernoulli's equation (Eq. 35) where h_g is the geometric head

$$\widehat{H} = h_g - \frac{\widehat{p}_L}{\rho_L g} \tag{35}$$

Essential BCs on the liquid phase include *impermeable boundaries* and *infiltration BC*. While the first is trivial, the second is more complex because the infiltration capacity of a soil depends on its hydraulic conductivity, and it can be solved in different ways. Bandara et al. [25] impose the infiltration velocity $\widehat{w}$ at the surface boundary nodes (BNs), i.e. nodes of the cell side which bound active and non-active nodes (Fig. 8). The infiltration velocity is applied only if the MPs located adjacent to the BNs are unsaturated. There is no control on the maximum infiltration velocity, i.e. the user should not apply a value of $\hat{w}$ larger than the maximum soil infiltration capacity $\widehat{w}_{max}$ if ponding is not allowed. The case $\widehat{w} > \widehat{w}_{max}$ will lead to pore pressures higher than zero at the boundary, meaning that a layer of free water is present above the free surface.

34

Martinelli et al. [31] and Ceccato et al. [30] apply a predictor-corrector scheme: liquid and solid velocities ($\tilde{v}_L$, $\tilde{v}_S$) are predicted assuming zero pressure at the infiltration boundary and then (eventually) corrected to ensure the prescribed infiltration rate $\widehat{w} = n_L(v_L - v_S)$. If the net infiltration discharge q_{net} (Eq. 36) is positive, ponding conditions occur, and if fluid accumulation above the boundary is not allowed (it must remain at zero pressure), no correction is necessary, meaning that the maximum soil infiltration capacity is met. If the net infiltration discharge is negative or liquid ponding is allowed above the surface, then the liquid velocity must be corrected to ensure the correct infiltration rate.

$$q_{net} = (n_L(\tilde{\mathbf{v}}_L^{t+\Delta t} - \tilde{\mathbf{v}}_S^{t+\Delta t}) - \widehat{\mathbf{w}}) \cdot \mathbf{n} \tag{36}$$

$\mathbf{n}$ is the normal direction at the node that is determined by means of the gradient of mass.

The two approaches differ in terms of velocity correction. Martinelli et al. [31] correct both liquid and solid velocity, while Ceccato et al. [30] correct only liquid velocity. The first one accurately ensures the conservation of momentum balance of the mixture at the boundary, i.e. the total stress remains constant at the ground level. The second one implicitly assumes that the relative acceleration between solid and liquid is negligible and that the effective stress at the boundary is constant and equal to zero.

In order to emphasize the difference between the two implementations on the results, a 1D infiltration example is used for comparison. A 1m-high soil column is considered with the material parameters listed in Tab. 6. For simplicity, the intrinsic permeability is assumed constant and equal to $k_L = 1 \cdot 10^{-11} m^2$,

35

corresponding to an hydraulic conductivity of $\kappa = 1.0 \cdot 10^{-4}$m/s. Van Genuchten SWRC is accounted (Eq. 23), with parameters $p_{ref} = 3kPa$, $\lambda = 0.7$, $S_{min} = 0.0$, $S_{max} = 1$.

Solid density [kg/m^3]	ρ_S	2700
Liquid density [kg/m^3]	ρ_L	1000
Porosity [-]	n	0.4
Liquid bulk modulus [kPa]	K_L	80000
Liquid dynamic viscosity [$kPa \cdot s$]	μ_L	$1 \cdot 10^{-6}$
Young modulus [kPa]	E	10000
Poisson ratio [-]	ν	0.2

Table 6. Material parameters for 1D infiltration example with applied infiltration velocity.

The column is discretised with 20 rows of 2 square triangular elements filled with 3 MPs each (Fig. 10a). The bottom and lateral boundaries are impervious, while a vertical infiltration rate $\widehat{w}_y = 1.0 \cdot 10^{-4}$ m/s is applied at the top boundary. An initial suction of 2kPa is assigned along the column at $t = 0$, which corresponds to an initial degree of saturation $S_{L0} = 0.85$.

The liquid infiltrates from the top and flows down through the column accumulating at the impervious bottom. Liquid suction decreases while soil saturates. As expected, the approaches proposed by Martinelli et al. [31] and Ceccato et al. [30] give different results. Due to the different correction of solid velocity, soil displacements at the column head are different. The approach from Ceccato et al. [30] results in a non-realistic solid velocity at the beginning of the calculation. This difference reduces with time, i.e. with the reduction of relative acceleration between liquid and solid. Despite the results obtained in terms of liquid pres-
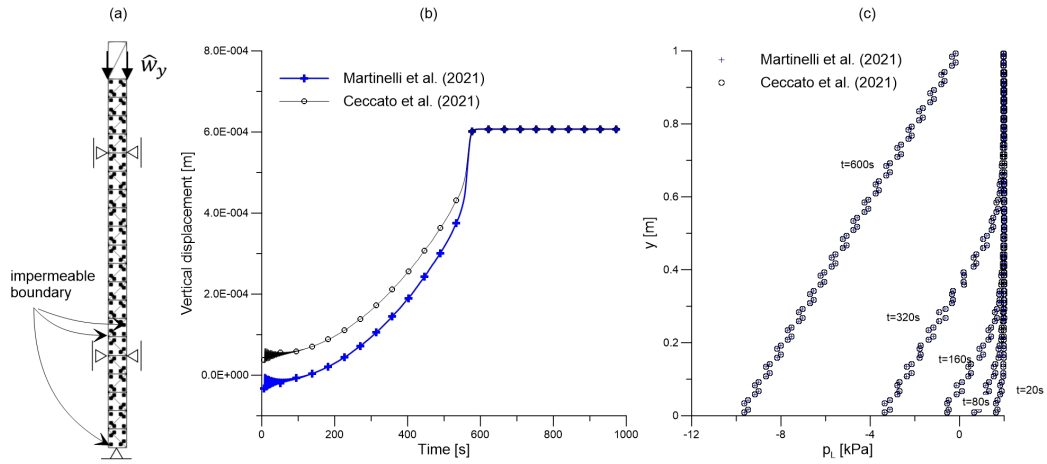
Fig. 10. 1D infiltration BC (a) geometry of the problem, (b) liquid pressure with depth, (c) displacement with time.

sures are very similar (Fig. 10b), the formulation from Martinelli et al. [31] is theoretically more accurate and therefore recommended.

In some cases, it is unknown if the boundary is an essential or a natural BC, for example, interface between soil and atmosphere where the fluid is free to exit at zero pressure when the soil is saturated. Still, it cannot enter when the soil is partially saturated. This boundary is called *potential seepage face*, and it is typical of the downstream surface of a dam or levee, or it can also arise on the reservoir side after a rapid drawdown of the water level.

Once more, Bandara et al. [25] solve this BC with the concept of *boundary layer*. If the boundary cell is fully saturated, i.e. $S_L = 1$ for all MP inside the cell, the pore pressure of all the MPs inside the cell is set to zero. If the boundary cell is unsaturated, i.e. there is at least 1 MP for which $S_L < 1$, then zero infiltration

37

rate is prescribed at the boundary nodes. The BC switches between natural and essential depending on the saturation level of the *boundary cell*. Ceccato et al. [30] solves the potential seepage face as a particular case of infiltration boundary condition in which $\widehat{w} = 0$ and applies the predictor-corrector scheme described previously. In this case, the BC switches between natural and essential depending on the infiltration discharge (Eq. 36). Similarly, the formulation by Martinelli et al. [31] can also be used for the same purpose.

4. Applications

All MPM formulations for partially saturated soils developed to simulate large-deformation problems were first validated using applications where soil displacement is limited. In general, the 1D infiltration problem is considered and the MPM results are compared with analytical solutions [24, 29], experimental data [25, 27, 16], or FEM calculations [33, 30, 31, 16].

For large-deformation applications, the MPM formulations for unsaturated soils were mainly used to study rainfall-induced slope failures, with particular emphasis on levees [30], embankments [24, 23] and landslides [25, 27, 32, 51, 16]. Ceccato et al. [30] looked at the displacement evolution of a levee after failure induced different boundary conditions, i.e. the rapid drawdown of the water level on the river side or an infiltration due to heavy rainfall, highlighting the importance of a large deformation tool for improving the accuracy of risk assessment. Yerro [24], Yerro et al. [23] described the instability of a embankment slope subjected to rain infiltration for a real case described in [52]. The model was able to show the development of the initial failure surface, and the progressive large strain deformation of the slope together with the dynamics of the motion characterised

38

by the history of displacement, velocity and acceleration of the unstable mass. The first rainfall-induced landslide using MPM considering a rainfall boundary condition was performed by Bandara et al. [25] for a case study inspired by the full-scale field test performed in Rüdlingen, Switzerland [53]. The model was able to show the negative effects on the stability of unsaturated slopes due to the presence of continuous rainfall and shallow soil cover to bedrock surface. Wang et al. [27] highlighted the importance of using coupled formulations for rainfall-induced landslides, as large difference in retrogressive failure modes was observed compared to the total stress analysis. More recently, the catastrophic event of the Fei Tsui Road landslide, occurred on 13 August 1995 in Hong Kong, was studied [32, 51, 54]. The first attempt was made by Lee et al. [32] where a linearly distributed suction with depth was initialized and the rainfall was applied as zero suction at the free surface. The evolution of the degree of saturation during the failure is illustrated in Fig. 11. Later on, Liu et al. [51] revised the initial conditions and simulated the failure process using a rainfall intensity equal to the saturated conductivity of the soil. Lastly, Cuomo et al. [54] simulated the complete rainfall event, exploring the failure process also in axisymmetric conditions.

Beside slope instability, other interesting applications using MPM for unsaturated soils are in the field of site investigation, soil-structure interaction (e.g. pile installation), excavation and trenching, and many others. For example, the role of unsaturated behaviour during soil characterization by means of site investigation (e.g. CPT, SPT, DMT, etc.) is relevant for soils above the water table. A new example of cone penetration test (CPT) in unsaturated soil is illustrated hereafter. The numerical simulation represents a penetration of a CPT, with radius $r_c = 3.6$ cm, in a virtual calibration chamber. The thickness of the soil domain is 1 m and
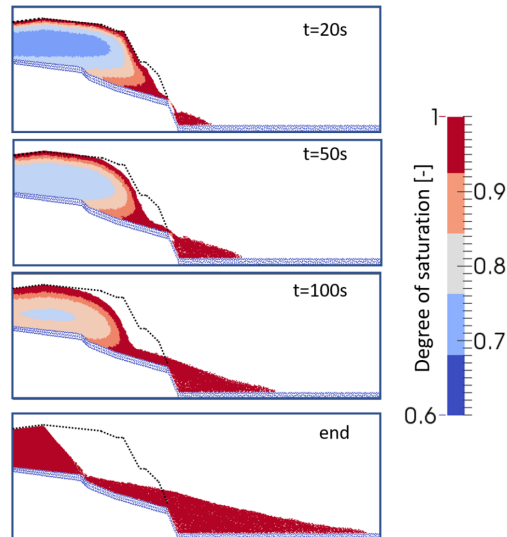
39

Fig. 11. Evolution of the degree of saturation during failure ([32])

the radius of 84 cm, loaded by 50 kPa constant in time. The computational mesh and numerical settings are equivalent to the one used by Martinelli and Galavi [55] for dry sand, but here unsaturated soil is considered. The soil behaviour is simulated using Mohr-Coulomb model with friction angle $\phi = 28°$ and zero cohesion. The full list of material parameters is in Table 6 and the water retention curve is the one for "clay" in Table 5. The contact between pile and penetrometer is perfectly smooth. The simulations are performed using the unsaturated formulation described in [31], with the additional assumption that soil-water relative movement is negligible.

Three different values of initial suction in the liquid pressure are considered (i.e. 0, 50 and 100 kPa), and the corresponding initial effective stress is then calculated to meet the equilibrium. The cone penetrates 40 cm into the soil sample and the cone resistance (q_c) is calculated as the ratio between the vertical reaction forces

40

on the cone and the area of the cross section of the penetrometer. The evolution of q_c during the penetration is illustrated in Fig. 12, where the cone resistance increases with the initial suction (u_0).

Fig.13 shows the distribution of pore water pressure in a close-up view of the computational mesh, close to the cone, at the penetration of 40 cm. It is observed that, if $u_0 = 0$, the soil domain is fully saturated and large pore water pressure is computed nearby the cone and along the shaft. In this case, a soil region of approximately 5 cone radii ($5r_c$) is affected by such a large pore water pressure change. As the initial suction increases ($u_0 = 50$ or 100 kPa), the degree of saturation decreases and the volumetric compressibility increases. It follows that, during the penetration, large pore pressures can still be developed below the cone, due to the large volumetric strains. However, the larger soil compressibility makes such a pore pressure changes concentrated in the vicinity of the penetrometer, whereas the rest of the domain remain almost unaffected.

Despite the relatively simple constitutive model used for to describe soil behaviour, this example highlights the important role of the initial suction and the unsaturated behaviour of soils on the measured cone resistance during site investigations.

As discussed in Sec. 3.1, all MPM formulations developed for unsaturated soil are implemented in explicit, typically suitable for fast processes (e.g. impacts, fast flows). For some of the applications which include long-term process (e.g. consolidation or creep), the very small time step, required by explicit integration schemes for stability criteria, makes the simulation extremely time consuming and sometimes unfeasible. The implementation of implicit MPM codes will overcome this issue.

41
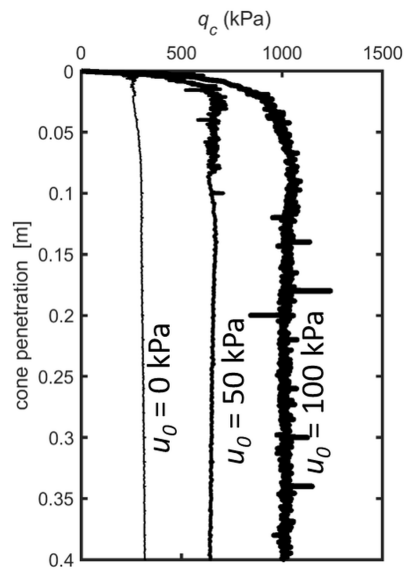
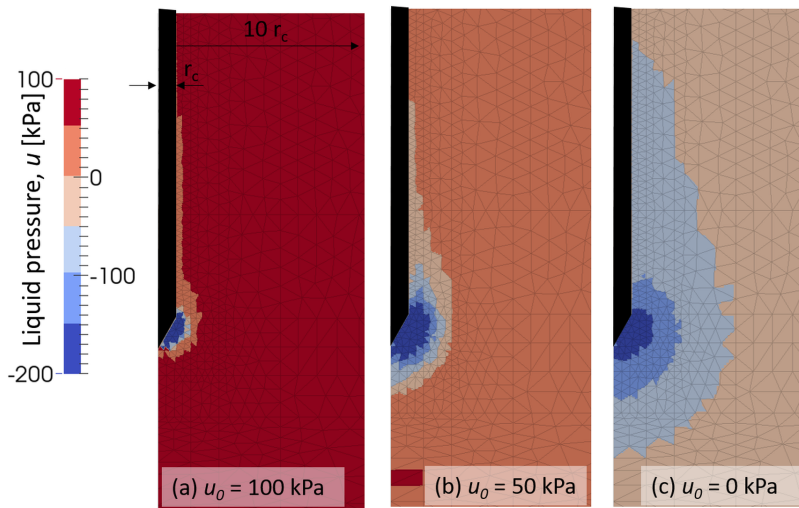**Fig. 12.** Cone resistance with depth. Effect of initial suction (u_0) in water.

Fig. 13. Cone penetration of 40 cm. Distribution of pore water pressure in the soil nearby the cone. Effect of initial suction (u_0) in water: (a) u_0 = 100 kPa; (b) u_0 = 50 kPa; (c) u_0 = 0 kPa. (negative values are in compression)

5. Conclusions

This paper presented an overview of the MPM formulations available for the simulation of unsaturated soils. Three-phase and two-phase formulations are proposed in the literature. The first one accounts for solid-liquid-gas interactions, while the second one neglects the pressure and density of the gas. While the three-phase formulations can be essential for the simulation of problems where pressure variations are important such as extremely rapid motions and explosion, the two-phase formulations are adequate for the study of problems where the gas pressure remains constant. The two-phase approach is computationally more efficient than the three-phase one because a reduced number of governing equations is required.

Most of the formulations include all inertial terms, which is ideal when dealing with dynamic problems. Neglecting the relative acceleration of the fluid with respect to the solid is not recommended in dynamic problems where relative movement between liquid and solid is expected. Finally, a few approaches neglect the gradient of fluid mass when evaluating the mass balances. This assumption is acceptable for most of the pressure gradients and SWRC present in many geotechnical applications, but it can induce errors when large gradients of pressure and degree of saturation are expected.

All MPM formulations currently available for unsaturated soils are integrated using explicit time schemes. The stability of the solution is limited by a critical time step. This paper presents the first investigation on the effects of degree of saturation (among other properties) on the stability of the solution. In general, the critical time step increases in unsaturated conditions. Practical recommendations are proposed based on the results to optimize the time step of the calculations.

43

⁶⁶⁵ Nevertheless, the implementation of implicit schemes is needed to study long-term

⁶⁶⁶ processes efficiently.

⁶⁶⁷ Despite the large number of geotechnical applications involving unsaturated soils,

⁶⁶⁸ a limited number of problems have been investigated, mainly focused on slope

⁶⁶⁹ stability and runout analysis. In this paper, preliminary results of a CPT model are

⁶⁷⁰ presented to illustrate the capabilities of unsaturated MPM in application involving

⁶⁷¹ soil-structure interaction.

6. Acknowledgements

7. Appendix

⁶⁷⁶ In this appendix, we present the steps followed to study the stability of the for-

⁶⁷⁷ mulation presented by Ceccato et al. [30] for the simulation of unsaturated soils.

⁶⁷⁸ Three different Δt_c criteria are obtained taking into the stability of (a) the coupled

⁶⁷⁹ system of momentum balance equations, (b) the momentum balance of the liquid

⁶⁸⁰ phase, and (c) the momentum balance of the mixture.

7.1. Stability of the coupled system of momentum balance equations

⁶⁸² The governing equations in the strong form considered are the liquid momentum

⁶⁸³ balance and the mixture momentum balance as in

$$\rho_L \mathbf{a}_L = \nabla p_L - \mathbf{f}_L^d + \rho_L \mathbf{g} \tag{37}$$

44

$$n_S\rho_S\mathbf{a}_S + n_L\rho_L\mathbf{a}_L = \nabla \cdot \boldsymbol{\sigma} + \rho_m\mathbf{g} \tag{38}$$

684 Additionally, the mass balance equation is considered to express the liquid pressure
685 as function of velocity (Eq.39). A linear elastic solid constitutive law (Eq.40) is
686 assumed to express effective stress as function of solid displacements. The sign
687 convention used expresses suction s as $s = -p_L$.

$$n\left(S_L\frac{\partial \rho_L}{\partial p_L} + \rho_L\frac{\partial S_L}{\partial p_L}\right)\frac{D^S p_L}{Dt} = \rho_L n S_L \text{div}(\mathbf{v}_S - \mathbf{v}_L) - \rho_L S_L \text{div}(\mathbf{v}_S) \tag{39}$$

$$d\boldsymbol{\sigma}' = \mathbf{E_c} \cdot d\boldsymbol{\varepsilon} \tag{40}$$

688 If a single node i is considered, the momentum balances per unit volume at time t_k
689 can be written as a system of second-order ordinary differential equations (ODE).
690 The homogeneous form for both equations is

$$\rho_L a_L^k + q_L v_L^k - q_L v_S^k + K_L u_L^k + \frac{(1-n)}{n}K_L u_S^k = 0 \tag{41}$$

$$(1-n)\rho_s a_S^k + nS_L\rho_L a_L^k + K_S u_S^k + \frac{(1-n)}{n}K_L u_S^k + K_L u_L^k = 0 \tag{42}$$

where

$$q_L = \frac{S_L n\mu_L}{k_L} \tag{43}$$

$$K_L = \frac{S_L}{L_i^2} \cdot \frac{1}{\left(\frac{dS_L}{ds} + \frac{S_L}{K_w}\right)} \tag{44}$$

$$K_S = \frac{E_c}{L_i^2} \tag{45}$$

691 In this notation K_w is the bulk modulus of the liquid, while K_L is a term which
692 includes K_w, S_L is the saturation degree, $\frac{dS_L}{ds}$ is the derivative of S_L respect to

45

suction, and L_i is the characteristic length of the element. The use of an Euler-Cromer time scheme leads to the following set of equations for the kinematic variables of liquid and solid phases.

$$v_L^{k+1} = v_L^k + \Delta t \, a_L^k \tag{46}$$

$$v_S^{k+1} = v_S^k + \Delta t \, a_S^k \tag{47}$$

$$u_L^{k+1} = u_L^k + \Delta t \, v_L^{k+1} \tag{48}$$

$$u_S^{k+1} = u_S^k + \Delta t \, v_S^{k+1} \tag{49}$$

From Eq.41 and Eq.42 it is possible to express accelerations as function of all the other terms as follows.

$$a_L^k = -\frac{q_L}{\rho_L} v_L^k + \frac{q_L}{\rho_L} v_S^k - \frac{K_L}{\rho_L} u_L^k - \frac{(1-n)}{n\rho_L} K_L u_S^k \tag{50}$$

$$a_S^k = -\frac{nS_L\rho_L}{(1-n)\rho_s} a_L^k - \frac{K_S}{(1-n)\rho_s} u_S^k - \frac{K_L}{n\rho_S} u_S^k - \frac{K_L}{(1-n)\rho_s} u_L^k \tag{51}$$

Now, the acceleration expressions (Eqs. 50 and 51) are substituted in the explicit time scheme set (Eqs. 48, 46, 49, 47).

$$u_L^{k+1} = u_L^k + \Delta t \left[v_L^k + \Delta t \left(-\frac{q_L}{\rho_L} v_L^k + \frac{q_L}{\rho_L} v_S^k - \frac{K_L}{\rho_L} u_L^k - \frac{(1-n)}{n\rho_L} K_L u_S^k \right) \right] \tag{52}$$

$$v_L^{k+1} = v_L^k + \Delta t \left(-\frac{q_L}{\rho_L} v_L^k + \frac{q_L}{\rho_L} v_S^k - \frac{K_L}{\rho_L} u_L^k - \frac{(1-n)}{n\rho_L} K_L u_S^k \right) \tag{53}$$

$$u_S^{k+1} = u_S^k + \Delta t \left[v_s^k + \Delta t \left(-\frac{nS_L\rho_L}{(1-n)\rho_s} a_L^k - \frac{K_S}{(1-n)\rho_s} u_S^k - \frac{K_L}{n\rho_S} u_S^k - \frac{K_L}{(1-n)\rho_s} u_L^k \right) \right] \tag{54}$$

46

$$v_S^{k+1} = v_S^k + \Delta t \left(-\frac{nS_L\rho_L}{(1-n)\rho_s} a_L^k - \frac{K_S}{(1-n)\rho_s} u_S^k - \frac{K_L}{n\rho_S} u_S^k - \frac{K_L}{(1-n)\rho_s} u_L^k \right) \quad (55)$$

The coefficients' matrix of the system of Eqs.52, 53, 54, 55 is evaluated to solve the eigenvalues problem,

$$det(A - \lambda I) = 0 \quad (56)$$

Thus, a quadratic equation for λ is obtained, where the terms $\geq \Delta t_c^3$ are neglected,

$$\lambda^2 + \lambda \left(\Delta t_c q_L Q - \frac{c\Delta t_c^2}{\rho_s} + \frac{K_L \Delta t_c^2}{\rho_L} - 2 \right) + \left(1 - \Delta t q_L Q \right) = 0 \quad (57)$$

If Eq.57 is solved for Δt_c by imposing $|\lambda| = 1$, it results in

$$\Delta t_c = \frac{-q_L Q + \sqrt{(q_L Q)^2 + 4 \left(\frac{K_L}{\rho_L} - \frac{c}{\rho_s} \right)}}{\left(\frac{K_L}{\rho_L} - \frac{c}{\rho_s} \right)} \quad (58)$$

Arranged in a more general form, it is equivalent to Eq.33 proposed by [24],

$$\Delta t_c = \frac{2}{\omega} \left[-\xi + \sqrt{\xi^2 + 1} \right] \quad (59)$$

where

$$\omega_c = \sqrt{\left(\frac{K_L}{\rho_L} - \frac{c}{\rho_s} \right)} = \frac{1}{L_i} \sqrt{\left[\frac{S_L}{\left(\frac{dS_L}{ds} + \frac{S_L}{K_w} \right)} \right] \left[\frac{1}{\rho_L} + \frac{1}{\rho_S} \left(\frac{1}{n} - S_L \right) \right] + \frac{E_c}{\rho_S(1-n)}}$$
$$(60)$$

$$\xi_c = \frac{q_L Q}{2\omega_c} = \frac{S_L n \mu_L}{2k_L \omega_c} \left[\frac{S_L n}{(1-n)\rho_S} + \frac{1}{\rho_L} \right] \quad (61)$$

47

7.2. Stability of the momentum balance of the liquid phase

Same procedure presented for the coupled system can be applied to study the stability of the momentum balance of the liquid phase. By considering the homogeneous form of Eq.41 (without the terms referring to the solid phase), we obtain

$$\rho_L a_L^k + q_L v_L^k + K_L u_L^k = 0 \tag{62}$$

The set of two ODEs (by considering the Euler-Cromer time scheme) is now

$$u_L^{k+1} = u_L^k + \Delta t \left[v_L^k + \Delta t \left(-\frac{q_L}{\rho_L} v_L^k - \frac{K_L}{\rho_L} u_L^k \right) \right] \tag{63}$$

$$v_L^{k+1} = v_L^k + \Delta t \left(-\frac{q_L}{\rho_L} v_L^k - \frac{K_L}{\rho_L} u_L^k \right) \tag{64}$$

The characteristic polynomial based on the resolution of the eigenvalues problem for Eqs. 63 and 64 is

$$\lambda^2 + \lambda \left(\frac{\Delta t_c q_L}{\rho_L} + \frac{K_L \Delta t_c^2}{\rho_L} - 2 \right) + \left(1 - \frac{\Delta t_c q_L}{\rho_L} \right) = 0 \tag{65}$$

Eq.65 solved for Δt_c gives

$$\Delta t_c = \frac{-\frac{q_L}{\rho_L} + \sqrt{\left(\frac{q_L}{\rho_L} \right)^2 + 4\frac{K_L}{\rho_L}}}{\frac{K_L}{\rho_L}} \tag{66}$$

Arranged in a more general form, it is equivalent to 33, where

$$\omega_L = \sqrt{\frac{K_L}{\rho_L}} = \frac{1}{L_i}\sqrt{\frac{S_L}{\rho_L\left(\frac{dS_L}{ds} + \frac{S_L}{K_w}\right)}} \qquad (67)$$

$$\xi_L = \frac{\left(\frac{q_L}{\rho_L}\right)}{2\omega_L} = \frac{S_L n\mu_L}{2k_L\omega_L}\frac{1}{\rho_L} \qquad (68)$$

7.3. Stability of the momentum balance of the mixture

Same procedure presented for the coupled system can be applied to study the stability of the momentum balance of the mixture. By considering the homogeneous form of Eq.42, we obtain

$$(1-n)\rho_S a_S^k + nS_L q_L v_S^k + \left[K_S + (1-n)\left(-S_L + \frac{1}{n}\right)K_L\right]u_S^k = 0 \qquad (69)$$

The set of 2 ODEs (by considering the Euler-Cromer time scheme) is now

$$u_S^{k+1} = u_S^k + \Delta t(v_s^k + \Delta t a_s^k) \qquad (70)$$

$$v_S^{k+1} = v_s^k + \Delta t a_s^k \qquad (71)$$

The characteristic polynomial (related to Eqs.70 and 71) is now

$$\lambda^2 + \lambda\left[P\Delta t_c^2 + \frac{S_L\Delta t_c n q_L}{(1-n)\rho_S} - 2\right] + \left[1 - \frac{S_L\Delta t_c n q_L}{(1-n)\rho_S}\right] = 0 \qquad (72)$$

where the term P is expressed as

$$P = \frac{1}{\rho_S}\left[\frac{K_S}{(1-n)} + \left(-S_L + \frac{1}{n}\right)K_L\right] \qquad (73)$$

49

If we solve Eq.72 for Δt_c we obtain

$$\Delta t_c = \frac{\left(-\frac{nS_L q_L}{(1-n)\rho_s} + \sqrt{\left(\frac{nS_L q_L}{(1-n)\rho_s}\right)^2 + 4P} \right)}{P} \tag{74}$$

Arranged in a more general form, it is equivalent to 33, where

$$\omega_M = \sqrt{P} = \frac{1}{L_i}\sqrt{\frac{1}{\rho_S}\left[\frac{E_c}{(1-n)} + \left(-S_L + \frac{1}{n}\right)\frac{S_L}{\left(\frac{dS_L}{ds} + \frac{S_L}{K_w}\right)} \right]} \tag{75}$$

$$\xi_M = \frac{\left(\frac{nS_L q_L}{(1-n)\rho_s}\right)}{2\omega_M} = \frac{S_L^2 n^2 \mu_L}{2(1-n)\rho_s k_L \omega_M} \tag{76}$$

References

[1] M. Pirulli, Numerical modelling of landslide runout, a continuum mechanics approach (2005).

[2] S. P. Pudasaini, A general two-phase debris flow model, Journal of Geophysical Research 117 (2012). doi:10.1029/2011JF002186.

[3] M. Pastor, T. Blanc, B. Haddad, V. Drempetic, M. S. Morles, P. Dutto, M. M. Stickle, P. Mira, J. F. Merodo, Depth averaged models for fast landslide propagation: mathematical, rheological and numerical aspects, Archives of Computational Methods in Engineering 22 (2015) 67–104.

[4] G. Qiu, J. Grabe, Explicit modeling of cone and strip footing penetration under drained and undrained conditions using a visco-hypoplastic model, Geotechnik 34 (2011) 205–217. URL: http://doi.wiley.com/10.1002/gete.201100004. doi:10.1002/gete.201100004.

[5] E. Oñate, S. R. Idelsohn, F. Del Pin, R. Aubry, the Particle Finite Element Method — an Overview, International Journal of Computational Methods 01 (2004) 267–307. URL: http://www.worldscientific.com/doi/abs/10.1142/S0219876204000204. doi:10.1142/S0219876204000204.

[6] L. N. Moresi, F. Dufour, H.-B. Muhlhaus, A lagrangian integration point finite element method for large deformation modeling of viscoelastic geomaterials., Journal of Computational Physics 184 (2003) 476–497. doi:https://doi.org/10.1016/S0021-9991(02)00031-1.

[7] H. H. Bui, R. Fukagawa, K. Sako, S. Ohno, Lagrangian meshfree particles method (sph) for large deformation and failure flows of geomaterial using elastic–plastic soil constitutive model, International Journal for Numerical and Analytical Methods in Geomechanics 32 (2008) 1537–1570. URL: https://onlinelibrary.wiley.com/doi/abs/10.1002/nag.688. doi:https://doi.org/10.1002/nag.688. arXiv:https://onlinelibrary.wiley.com/doi/pdf/10.1002/nag.688.

[8] D. Sulsky, Z. Chen, H. Schreyer, A particle method for hystory-dependent materials, Computer Methods in Applied Mechanics and Engineering 118 (1994) 179–196.

[9] K. Soga, E. Alonso, A. Yerro, K. Kumar, S. Bandara, Trends in large-deformation analysis of landslide mass movements with particular emphasis on the material point method, Géotechnique 66 (2016) 248–273. URL: http://dx.doi.org/10.1680/jgeot.15.LM.005]http://www.icevirtuallibrary.com/doi/10.1680/jgeot.15.LM.005. doi:10.1680/jgeot.15.LM.005.

51

[10] F. H. Harlow, The particle-in-cell method for numerical solution of prob-
lems in fluid dynamics (1962). URL: https://www.osti.gov/biblio/
4769185. doi:10.2172/4769185.

[11] F. Ceccato, L. Beuth, P. A. Vermeer, P. Simonini, Two-phase material point
method applied to the study of cone penetration, Computers and Geotech-
nics 80 (2016) 440–452. URL: http://linkinghub.elsevier.com/
retrieve/pii/S0266352X16300477http://dx.doi.org/10.1016/
j.compgeo.2016.03.003. doi:10.1016/j.compgeo.2016.03.003.

[12] L. Zambrano-Cruzatty, A. Yerro, Numerical simulation of a free fall pen-
etrometer deployment using the material point method, Soils and Foun-
dations 60 (2020) 668–682. URL: https://www.sciencedirect.com/
science/article/pii/S0038080620336179. doi:https://doi.org/
10.1016/j.sandf.2020.04.002.

[13] M. Martinelli, V. Galavi, Investigation of the material point method in the
simulation of cone penetration tests in dry sand, Computers and Geotechnics
130 (2021) 103923. URL: https://www.sciencedirect.com/science/
article/pii/S0266352X20304869.

[14] A. Yerro, A. Rohe, K. Soga, Modelling internal erosion with the material
point method, in: 1st International Conference on the Material Point Method,
MPM 2017, volume 00, 2017, pp. 1–8. doi:10.1016/j.proeng.2017.01.
048.

[15] A. Yerro, K. Soga, J. Bray, Runout evaluation of Oso landslide with the

material point method, Canadian Geotechnical Journal 14 (2018) 1–14. doi:10.1139/cgj-2017-0630.

[16] X. Lei, S. He, X. Chen, H. Wong, L. Wu, E. Liu, A generalized interpolation material point method for modelling coupled seepage-erosion-deformation process within unsaturated soils, Advances in Water Resources 141 (2020) 103578. doi:10.1016/j.advwatres.2020.103578.

[17] E. J. Fern, Modelling tunnel-induced deformations with the material point method, Computers and Geotechnics 111 (2019) 202–208. URL: https://doi.org/10.1016/j.compgeo.2019.03.017. doi:10.1016/j.compgeo.2019.03.017.

[18] E. J. Fern, A. Rohe, K. Soga, E. E. Alonso, The Material Point Method for Geotechnical Engineering: A Practical Guide, CRC Press, 2019.

[19] A. Yerro, A. Rohe, Fundamentals of the Material Point Method, in: J. Fern, A. Rohe, K. Soga, E. Alonso (Eds.), The Material Point Method for Geotechnical Engineering, CRC Press, 2019, pp. 101–124. doi:10.1201/9780429028090-6.

[20] S. S. Bandara, Material Point Method to simulate Large Deformation Problems in Fluid-saturated Granular Medium, {PhD} {t}hesis, Ph.D. thesis, Cambridge, UK, 2013.

[21] M. Martinelli, Soil-water interaction with Material Point Method. Double-Point Formulation, Technical Report, Report on EU-FP7 research project MPM-Dredge PIAP-GA-2012-324522., 2016.

[22] E. J. Fern, D. A. de Lange, C. Zwanenburg, J. A. M. Teunissen, A. Rohe, K. Soga, Experimental and Numerical investigations of dyke failures involving soft materials, Engineering Geology 219 (2016) 130–139. URL: http://linkinghub.elsevier.com/retrieve/pii/S0013795216302198http://dx.doi.org/10.1016/j.enggeo.2016.07.006. doi:10.1016/j.enggeo.2016.07.006.

[23] A. Yerro, E. E. Alonso, N. M. Pinyol, The material point method for unsaturated soils, Geotechnique 65 (2015) 201–217. URL: http://www.icevirtuallibrary.com/doi/10.1680/geot.14.P.163. doi:10.1680/geot.14.P.163.

[24] A. Yerro, MPM modelling of landslides in brittle and unsaturated soils, Phd thesis, Univestitat Politecnica de Catalunya, Spain, 2015.

[25] S. Bandara, A. Ferrari, L. Laloui, Modelling landslides in unsaturated slopes subjected to rainfall infiltration using material point method, International Journal for Numerical and Analytical Methods in Geomechanics 40 (2016) 1358–1380.

[26] B. Wang, P. Vardon, M. Hicks, Investigation of retrogressive and progressive slope failure mechanisms using the material point method, Computers and Geotechnics 78 (2016) 88–98. URL: http://linkinghub.elsevier.com/retrieve/pii/S0266352X16300891. doi:10.1016/j.compgeo.2016.04.016.

[27] B. Wang, P. J. Vardon, M. A. Hicks, Rainfall-induced slope collapse with coupled material point method, Engineering Geology 239 (2018) 1–12. URL:

https://doi.org/10.1016/j.enggeo.2018.02.007. doi:10.1016/j.
enggeo.2018.02.007.

[28] X. Lei, W. Solowski, Mpm simulation of fine particle migration process
within unsaturated soils, in: Proceedings of the 2nd International Conference
on the Material Point Method for Modelling Soil-Water-Structure Interaction
(MPM 2019), 2019.

[29] F. Ceccato, V. Girardi, A. Yerro, P. Simonini, Evaluation of dynamic explicit
MPM formulations for unsaturated soils, in: E. Oñate, M. Bischoff, D. Owen,
P. Wriggers, T. Zohdi (Eds.), Particles 2019, Barcelona, 2019.

[30] F. Ceccato, A. Yerro, V. Girardi, P. Simonini, Two-phase dynamic MPM
formulation for unsaturated soil, Computers and Geotechnics 129 (2021)
103876. URL: https://doi.org/10.1016/j.compgeo.2020.103876.
doi:10.1016/j.compgeo.2020.103876.

[31] M. Martinelli, W.-L. Lee, C.-L. Shieh, S. Cuomo, Rainfall Bound-
ary Condition in a Multiphase Material Point Method (2021) 303–309.
doi:10.1007/978-3-030-60706-7_29.

[32] W. Lee, M. Martinelli, C. L. Shieh, Modelling rainfall-induced land-
slides with the material point method: the Fei Tsui Road case, in: Pro-
ceedings of the XVII ECSMGE-2019 Geotechnical Engineering foundation
of the future ISBN 978-9935-9436-1-3, Knii 1996, 2019. doi:10.32075/
17ECSMGE-2019-0346.

[33] F. Ceccato, V. Girardi, P. Simonini, Developing and testing multiphase mpm
approaches for the stability of dams and river embankments, in: Conference

852 of the Italian Association of Theoretical and Applied Mechanics, Springer,
853 2019, pp. 2179–2195.

854 [34] A. Yerro, A. Rohe, K. Soga, Modelling Internal Erosion with the Ma-
855 terial Point Method, Procedia Engineering 175 (2017) 365–372. URL:
856 http://dx.doi.org/10.1016/j.proeng.2017.01.048. doi:10.1016/
857 j.proeng.2017.01.048.

858 [35] M. Nuth, L. Laloui, Effective stress concept in unsaturated soils: Clarification
859 and validation of a unified framework, International journal for numerical
860 and analytical methods in Geomechanics 32 (2008) 771–801.

861 [36] A. W. Bishop, The principle of effective stress, Teknisk ukeblad 39 (1959)
862 859–863.

863 [37] E. E. Alonso, A. Gens, A. Josa, A constitutive model for par-
864 tially saturated soils, Géotechnique 40 (1990) 405–430. URL: https:
865 //doi.org/10.1680/geot.1990.40.3.405. doi:10.1680/geot.1990.
866 40.3.405. arXiv:https://doi.org/10.1680/geot.1990.40.3.405.

867 [38] A. Yerro, E. E. Alonso, N. M. Pinyol, Run-out of landslides in brittle soils.
868 A {MPM} analysis, in: K. et al. Soga (Ed.), Geomechanics from micro to
869 macro, London: Taylor and Francis, 2014, pp. 977–982.

870 [39] M. Van Genuchten, A closed-form equation for predicting the hydraulic
871 conductivity of unsaturated soils, Soil science society of America journal 44
872 (1980) 892–898.

873 [40] D. Hillel, Soil and water – physical principles and processes, Academic press,
874 London (UK), 1971.

[41] Y. Mualem, Hysteretical models for prediction of the hydraulic conductivity of unsaturated porous media, Water Resources Research 12 (1976) 1248–1254. URL: http://doi.wiley.com/10.1029/WR012i006p01248. doi:10.1029/WR012i006p01248.

[42] E. E. Alonso, A. Lloret, Evolution in time of the reliability of slopes in partially saturated soils, in: Pitagora (Ed.), Applications of Statistics and Probability in Soil and Structural Engineering, Firenze, 1983, pp. 1363–1376.

[43] A. Yerro, E. Alonso, N. Pinyol, Modelling large deformation problems in unsaturated soils, in: E-UNSAT 2016, volume 9, 2016, pp. 1–6. doi:10.1051/e3sconf/20160908019.

[44] M. M. J. Mieremet, Numerical stability for velocity-based 2-phase formulation for geotechnical dynamic analysis, Report 15-03, {ISSN} 1389-6520, Reports of the Delft Institute of Applied Mathematics, Delft University of Technology, Delft, The Netherlands, 2015.

[45] I. K. J. Al-Kafaji, Formulation of a Dynamic Material Point Method (MPM) for Geomechanical Problems, Ph. d. thesis, Ph.D. thesis, University of Struttgart, Germay, 2013. URL: http://elib.uni-stuttgart.de/opus/volltexte/2013/8549/.

[46] C. Hirsch, Numerical Computation of Internal and External Flows: The Fundamentals of Computational Fluid Dynamics, Elsevier Science, 2007.

[47] Http://www.anura3d.com/, ANURA3D, 2016. URL: http://mpm-dredge.eu/.

[48] N. Lu, W. Likos, K. (Firm), Unsaturated Soil Mechanics, Wiley, 2004. URL: https://books.google.com/books?id=Rv1RAAAAMAAJ.

[49] F. Ceccato, P. Simonini, Numerical Features Used in Simulations, in: J. Fern, A. Rohe, K. Soga, E. Alonso (Eds.), The Material Point Method for Geotechnical Engineering, CRC Press, 2019, pp. 101–124. doi:10.1201/9780429028090-6.

[50] V. Girardi, A. Yerro, F. Ceccato, P. Simonini, Modeling large deformations in water retention structures with an unsaturated MPM approach, Geotechnical Engineering (2021). doi:10.1680/jgeen.21.00059.

[51] X. Liu, Y. Wang, D. Li, Numerical simulation of the 1995 rainfall-induced fei tsui road landslide in hong kong: new insights from hydro-mechanically coupled material point method, Landslides 17 (2020) 2755–2775. doi:10.1007/s10346-020-01442-2.

[52] E. E. Alonso, N. M. Pinyol, P. A. M., Geomechanics of Failures. Advanced Topics, Springer, 2010.

[53] A. Askarinejad, Failure Mechanisms in Unsaturated Silty Sand Slopes Triggered by Rainfall, Phd thesis, ETH Zurich, 2013.

[54] S. Cuomo, A. Di Perna, M. Martinelli, Modelling the spatio-temporal evolution of a rainfall-induced retrogressive landslide in an unsaturated slope, Engineering Geology (2021) 106371. URL: https://www.sciencedirect.com/science/article/pii/S0013795221003823. doi:https://doi.org/10.1016/j.enggeo.2021.106371.

[55] M. Martinelli, V. Galavi, Investigation of the material point method in the simulation of cone penetration tests in dry sand, Computers and Geotechnics (2020) 103923.